A STUDY OF PREFERRED ORIENTATIONS IN GOLD/SILICA/SILICON INTERFACES

SANJEEV VASISHT

A study of preferred orientations in Gold/Silica/Silicon interfaces

By

©Sanjeev Vasisht

B. Tech (Honors), I.I.T Kharagpur, India

A thesis submitted to the school of graduate studies in partial fulfillment of the requirements for the degree of Master of Engineering

Faculty of Engineering and Applied Science

Memorial University of Newfoundland

June 2005

St. John's Newfoundland Canada

Abstract

The interfacial structure of Au (metal) on Si(100), Si(111) and SiO_2 (non-metal) substrates are studied owing to their immense use in the microelectronic industry. The interface study is important for understanding the structure-property relationships in materials.

The final orientation distribution of metallic crystalline films grown on these amorphous/crystalline, amorphous substrates namely $Au/SiO_2/Si(100)$; $Au/SiO_2/Si(111)$; Au/SiO_2 is strongly influenced by preferred orientations. Preferred orientations can be due to atomic mismatch, interface defects, anisotropy in crystal nucleation, growth rates, kinetics, etc. Geometric models have tried to explain the phenomena occurring at the interface to some extent.

The orientation of Au{111}, close-packed planes was found to be of low energy as the annealing temperature was increased, also a greater numbers of Au peaks of higher intensity were observed, implying more rotation of Au particles into preferred orientations of low energy. Orientations were observed to be influenced by Silicon substrates across native oxide of 20-35 Å; this suggests the effect of long range ordering via interfacial layer. The XRD/Pole figures, SEM/EDS and AFM were the tools used to characterize the prepared samples. The average crystallite size was determined by various methods on stage III samples and it was found to be fairly consistent.

Acknowledgements

I would like to thank my thesis supervisor Dr. John Shirokoff for his constant encouragement, inspirational talks and appropriate guidance during my enriching stay at Memorial University of Newfoundland. I would also like to thank him for extending his help in operating the XRD, SEM and Tube furnace facilities. He introduced me to the field of "metal non-metal" interfaces and I was truly fascinated by his style of learning and research.

Thanks are due to Dr. Erika Merschrod for her time with the AFM and Lisa Lee for helping me out with the SEM.

I am forever indebted to my parents, family members and friends for constant encouragement and support. Last but not the least I am grateful for the financial support from my supervisor's NSERC grant and a fellowship from the School of Graduate Studies, Memorial University of Newfoundland.

Contents

List of Figures

List of Tables

Chapter 1

Introduction

1.1 Purpose and Motivation behind Interface Studies

Internal interfaces are extended defects in materials including grain boundaries and interphase boundaries, found in every natural or artificially produced material. Integrated-circuit technology is an area of research encompassing several different materials and thus interfaces play a crucial role in the performance of these devices. Production of microelectronic devices, multiphase and composite materials requires a study of the interface which is paramount in understanding the structure-property relationships in materials [1]. Orientation relationships between the two phases and the defect structure at the interface are important factors controlling the structure-property relationships in crystalline systems.

Extreme service conditions sometimes prevail; such as high temperature, aggressive surrounding media and electromigration at high current densities. Thus the structure of interface must be regarded from the point of view of the whole complexity of the

thermodynamic conditions at the time of fabrication, growth and exploitation of the device, generally in thermodynamic non-equilibrium [2-5]. Therefore, interface engineering is an important field in materials engineering. Factors like orientation relationship, interfacial misfit and interface kinetics play a key role in the control of internal interface. Interface properties depend upon a large number of independent variables. This makes the study of interface properties very complex. The structure of an interface and its dependence on the independent variables makes the task of understanding interfaces even more challenging.

For the situation where the interface is formed between crystals with similar bonding we come across misfit dislocations at the interface and these are consistent with the concept of atomic matching. In such crystals impurity distribution at the interface has a role to play at the grain boundaries.

For the system where the interface is formed between crystals with different bonding, the situation becomes more complicated [1-5, 7]. To explain these interfaces numerous models have been proposed. Mostly they are geometrical models based on crystallographic orientation relationships. Geometric models have not been very successful in explaining the phenomena occurring at the interphase boundaries. Thus there is a constant debate as to what explains the interfacial phenomena best and thus new models have come along in quest of providing a better explanation.

Researchers have followed approaches different from geometrical models by including parameters other than geometry. This has been done by investigation of new interface systems in order to establish new models which can explain the preferred orientations at the interface. An attempt in this direction was made when electronic effects were considered to form and transform the structure of the interface and the orientation relationships [6]. Space charges were believed to influence the structure of the interface of a metal/ionic crystal system. A long range force is thus believed to exist across thin amorphous interlayer in some metal non-metal systems. This reason was not accepted completely for explaining preferred orientations across amorphous interlayers. Perhaps surface topology and/or pressure effects play a greater role than originally considered.

It is very important to understand the reason behind this phenomena of Au settling into the preferred orientations and to do this we studied orientation relationships for the following systems, $Au/SiO_2/Si$ (100), $Au/SiO_2/Si$ (111) and Au/SiO_2.

1.2 Overview of Thesis

This chapter is followed by the Literature Review section (chapter 2). This will include a discussion on crystalline-crystalline and crystalline-amorphous systems based on the concepts of interfacial energy, thermodynamics, epitaxial growth and lattice misfit considerations.

The Experimental section (chapter 3) in this thesis includes a brief discussion on the historical development of sphere-plate technique, substrates used, experimental procedure and the characterization techniques used. The techniques used for characterizing sphere-plate samples, X-ray Diffraction (XRD)-Pole Figure Determination, Scanning Electron Microscope (SEM)-Energy Dispersive Spectroscopy (EDS) and Atomic Force Microscope (AFM) are discussed in some details.

The Results and Discussion (chapter 4) has all the results obtained for our prepared sphere-plate samples. The results obtained from XRD-Pole Figures, SEM-EDS and AFM are then discussed individually. This is followed by comparisons amongst various results and its interpretation. These results were found to be consistent with the findings in the literature review.

The Conclusions (chapter 5) gives a brief account of interpretation of results.

Chapter 2

Literature Review

2.1 Theory

Determination of the nature of linear defects from contrast observations in electron microscope or field-ion microscope is a tedious process. The detection and analysis of defects is therefore in most cases done by macroscopic observations of parameters such as the misorientation of grains and overall boundary plane and partially from detailed observations of the defects or the structure of the boundaries themselves [7].

One common feature of all theories proposed to explain the phenomena occurring at the phase boundaries or interface is that for some given misorientation between two grains there exists at least one specific grain boundary plane with a specific low energy structure which the interface tries to attain. Any change from this low energy configuration due to misorientation of grains, plane or structure would result in a high energy and unstable configuration. There are situations where such changes in the energy configuration from a lower to higher value is required and this might be due to maintaining macroscopic relationship between grains. Therefore in these cases the interface retains the lowest

energy configuration over most of its area and the residual misfits will be localized to defects in the interface.

2.1.1 CSL Model

Properties observed for boundaries between grains with certain orientation relationships, (e.g. changed migration rate) form the experimental basis for the coincident site lattice (CSL) model. CSL relationship is characterized either by the reciprocal of density of common lattice points, Σ, [8] or by the angle of rotation around the axis with the lowest Miller indices (see figure 2.1). Perfect crystal matching has lattice points coincident or Σ=1. A simple twin has the next highest coincidence with Σ=3. In CSL theory the low energy grain structure is usually considered to contain the highest possible density of common lattice points.

A 3D CSL has an angle of misorientation θ, given by the expression [9-11]:

$$\theta = 2\tan^{-1}\left(\frac{y}{x}\right)\sqrt{N}$$

All possible cubic systems can be described by the function:

$$\Sigma = x^2 + Ny^2$$

Where x and y are integers.

$$N = h^2 + k^2 + l^2$$

h, k and l are the miller indices of the plane or the direction perpendicular to that plane,

A CSL is always generated for a rotation of 180° about a rational direction of <hkl>. While using the above equations for determining Σ, we keep on dividing the number by 2 until we get an odd number.

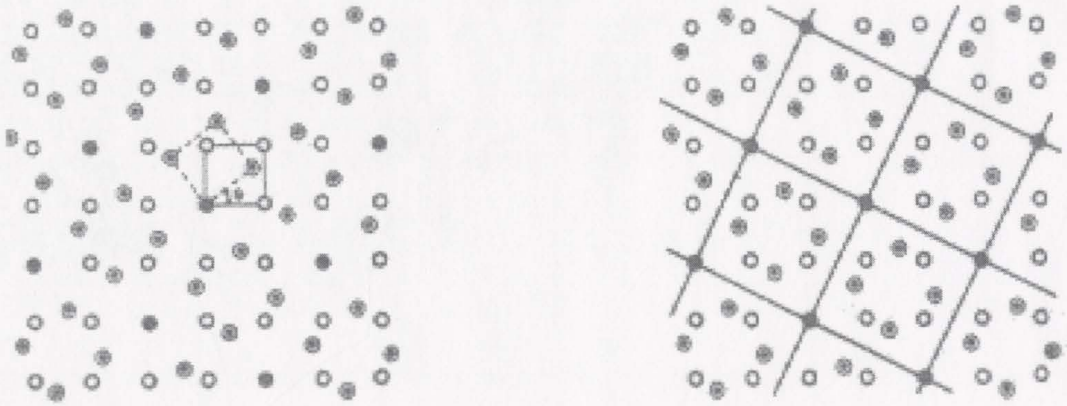

(a) (b)

Figure 2.1: Schematic of two superimposed crystal lattices showing rotation effect and CSL: (a) pattern produced by rotating two cubic crystals 36.9° about [001], (b) Σ=5 CSL pattern outlined [9].

The CSL model has some limitations and to understand that two kinds of deviations from the ideal CSL boundary must be considered. Firstly, due to a misorientation of the two grains from the ideal position and secondly, due to deviation of the interface from the low energy plane.

A network of structural dislocations superimposed on the coincidence boundary accommodate for the small misorientations due to coincidence relationships. Bollmann

gave a formal theory to explain such dislocations [12]. The lattice points must change when the Burgers vector b is introduced and then any two points connected by b in the original configuration will occupy a common site, implying that the step in the boundary must be associated with a dislocation if the low energy structure is to be maintained on both sides of the dislocation [13]. A general misorientation will be in the 3D space and thus require three non-coplanar Burgers vectors to define it. The length of b is inversely proportional to the reciprocal density of common lattice points, Σ and is proportional to $\Sigma^{-1/2}$.

Coincidence boundary is said to be at its lowest energy configuration when it lies in the most densely packed plane of the superlattice, formed by placing atoms at the lattice points of the two interpenetrating lattices after rotation about its axis. The energy of this boundary is supposed to be higher when it lies on the planes with lower densities of such sites. If a boundary is forced to lie at an angle to the close packed plane in the coincidence lattice, it will tend to take up a stepped structure such that it has a maximum area in the close packed planes of the coincident lattice [8].

The CSL model depends on the presence of coincident sites. The number of such coincident sites will decrease with increase in the value of Σ, [12]. The model makes no sense for the situation where for the upper limit of Σ, the difference between the energy of coincidence boundary and energy of a "random" boundary is negligible.

The CSL model has been applied successfully to grain boundaries and interphase boundaries where orientation relationships were described as the cusps in the interfacial energy versus misorientation. Interfacial structure can be understood in terms of atomic mismatch between two crystals across the interface for any degree of misorientation or rotation about the axis using this geometric model.

2.1.2 O-Lattice Model

The O-lattice model or lattice of origins model is a geometric perspective of interface structure. It follows the CSL concept in a generalised way to assume ordered interfaces and the points, lines and planes of coincidence are called the O-points, O-lines and O-planes respectively (see figure 2.2). The O-lattice changes continuously between the discreet CSL's [11]. Misfits between O-points is accommodated by dislocations by forming low energy structure, these points are the one with minimum strain energies of exact matching between two interpenetrating lattices. All CSL's can be described as superlattices of certain O-lattices as CSL is composed of only coincident lattices and since all O-points are not coincident. Thus all CSL points are regarded as O-points but vice-versa is not always true. Calculations reveal that not all O-points are associated with low energy [14], thus we conclude that this is entirely a geometrical concept so we can make no prediction about energetic significance of different kinds of O-points.

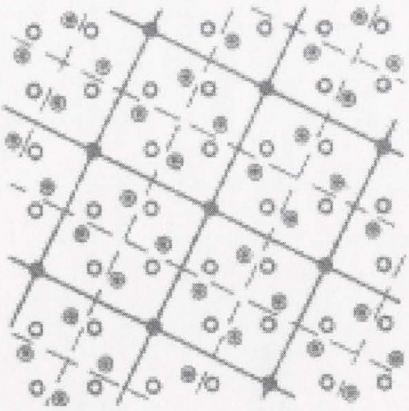

Figure 2.2: The O-lattice: CSL lattice plus the dashed lines [9].

2.1.3 DSC Model

The displacement shift complete model can be understood by considering the case when two interpenetrating point lattices stay in coincidence orientation but not necessarily in coincidence position. Thus it becomes a translation of the second lattice with respect to the first lattice such that there is no change in the structure and pattern (see figure 2.3). The lattice formed by this translation is the DSC lattice [11].

This model is a variation to the CSL model and involves a great deal of understanding of dislocation structures at the interfaces. The model describes the internal interfaces as an internal interface consisting of fit and misfit regions across the boundary. The regions of fit are patches of partial lattice matching across the boundary and the regions of misfit are line defects having dislocation, step or ledge character.

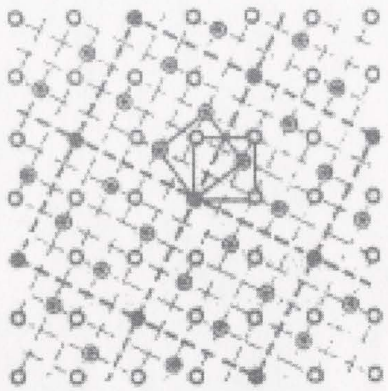

Figure 2.3: The DSC lattice of Σ=5 patterns: [9].

Thus DSC model provides a method to quantify the nature of variations in defects such as ledges occurring at grain and interphase boundaries.

2.1.4 Plane Matching Model

The plane matching (PM) model is applied to interfaces of low index which are misoriented in such a way that their continuity of parallel planes are restored by a set of periodic defects (see figure 2.4). This is possible in a crystal system under the condition that the atom planes are close packed, i.e. {100}, {110} and {111} in fcc crystals.

The boundary plane is not very crucial in this model. A PM boundary is regarded as a limiting case of a CSL model. In the PM model the boundaries created are all considered to be of low energy and low-indexes as compared to the CSL model where only the ones at specific misorientations are of low energy configuration.

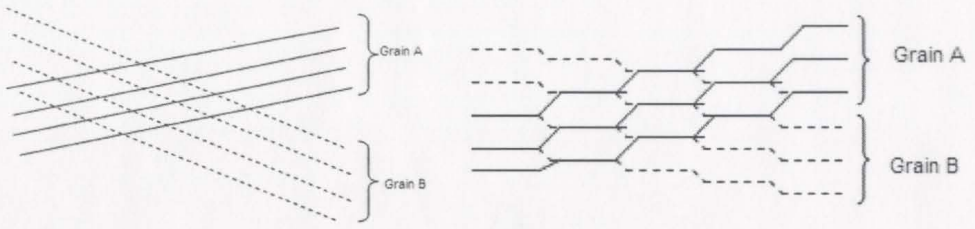

(a) (b)

Figure 2.4: The Plane matching model for twist misfits: (a) unrelaxed planes, (b) relaxed planes [7].

It has been demonstrated that the PM model can predict the spacing and orientation for high angle grain boundaries in fcc metals [15].

2.1.5 Wulff Construction

A small crystal at equilibrium has a specific shape at a particular temperature. Assuming net force on it is zero we have [16]:

$$\gamma dA = 0$$

A polycrystalline thin film on a substrate is an example of non-equilibrium since the crystallites are not satisfying the above equation. The Wulff's theorem for equilibrium condition corresponds to one crystal having {hkl} face exposed such that:

$$\int \gamma(hkl)\, dA(hkl) \text{ is minimum.}$$

Where, γ(hkl) is the surface energy and is a function of crystal orientation [17-18], dA(hkl) is the differential area perpendicular to <hkl>. Thus to deduce the equilibrium shape of a small crystal we require to know γ(hkl) and vice-versa (figure 2.5).

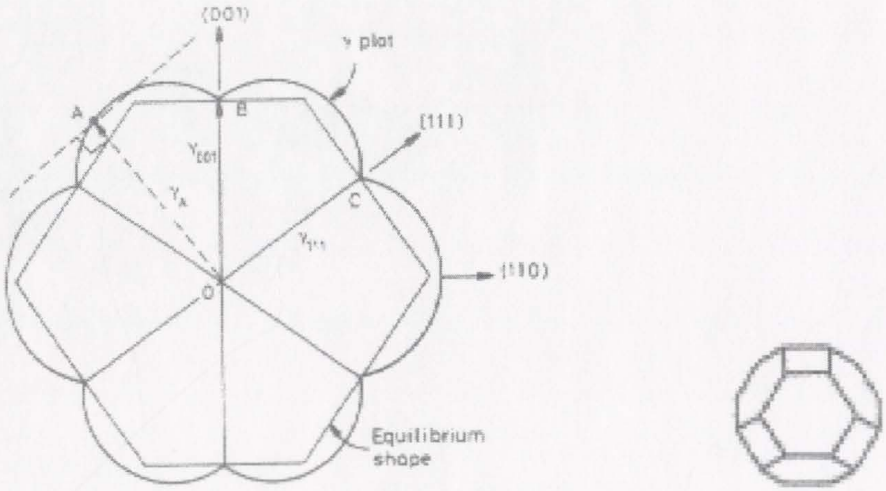

(a) (b)

Figure 2.5: Polar γ-plot in 2D: (a) for f.c.c crystal oriented along $<1\bar{1}0>$, (b) equilibrium shape of the crystal derived from Wulff plot in 3D, [11].

The Terrace-ledge-kink (TLK) model is proposed to facilitate representation of surface energies as a function of orientation [16]. The TLK model is used to explain the formation of Kossel crystal where the kink site is a repeatable step and moving kink around does not change the number of T, L and K atoms or the energy of the surface. TLK model helps in developing atomic structure of surface and thus facilitates understanding temperature dependence of surface energy in a greater depth.

Wulff's construction is a polar diagram of $\gamma(\theta)$ or the γ-plot. Wulff's construction is a problem in calculus of variation and its derivation to determine the mechanical stability of a particular orientation was originally flawed [18]. The equilibrium for any crystal according to Wulff's theorem occurs when $\int \gamma dA$ is minimum, i.e. when one draws the perpendicular through $\gamma(\theta)$ and takes the inner envelope. For Kossel Crystal the γ-plot shows that the equilibrium form is a cube. For more complicated crystals, equilibrium forms can be a polyhedron and in these cases sharp cusps exist on the Wulff plot. The width of the crystal facets is inversely proportional to the surface energy as seen in the figure. The deepest cusps on the γ-plots represent the singular faces (figure 2.5 (b)). High energy faces may or may not exist on the γ-plot. Between singular faces rounded regions exist where the faces are rough.

Whether an orientation is mechanically stable or not depends on the surface stiffness:

$$\gamma(\theta) + \frac{d^2\gamma(\theta)}{d\theta^2} > \text{or} < 0$$

The case of negative stiffness leads to faceting [16]. This condition can occur at a 2D surface or along steps or dislocations on a 1D surface in elastically anisotropic media having unstable directions [19]. Facets are generally low-energy and low-indexed planes formed by breaking of an arbitrarily orientated, originally flat surface into hill-and-valley structures composed of two or more facets. A flat surface on the equilibrium shape of the Wulff's construction represents stability (figure 2.5 (b)). Surfaces of other orientations

are unstable and will show faceting and, if kinetically feasible, the surface will break down into flat crystal surfaces.

The equilibrium shape and surface energy anisotropy of crystals was determined experimentally by annealing small single crystals in ultrahigh vacuum and observing the phenomena of faceting and the shape of the crystal as a function of temperature. For fcc lead and gold experiments have been done and have been found to be informative because they do not dissolve carbon from the substrate. SEM studies of lead particles on graphite show faceting along the planes (111) and (100). The surface energies can be measured by measuring the width of facets and it was found to be inversely proportional to temperature. The measurements for lead and gold over graphite [20-21] show that maximum surface energy anisotropy at 200°C and 1000°C are 6% and 3.4% respectively along <113> and <110> directions. The anisotropy between (111) and (100) was less than 2% for lead and 1.9% for gold deposits.

Thus it is evident from above discussion that shape of the balls is influenced by γ-plot and surface energy anisotropy. Also it is know from liquid-solid interface studies that wetting angle/contact angle is influenced by the density of defects and impurities at the interface which also affects the growth pattern. The equilibrium form of a small crystal on a substrate includes close-packed faces, i.e. {111}, {100}, {110} for f.c.c metal crystals and {110}, {100} for b.c.c metal crystals.

2.2 Crystalline-Crystalline Interfaces

For crystalline-crystalline studies the structure and properties are controlled mainly by the orientation relationships between the crystals. The defect structure at the interface is also very important. The phenomena at the interphase boundary can be best explained by the interfacial energy concept. The energy of an interphase boundary depends on many physical/chemical/geometrical factors such as the atomic mismatch at the interface, type of bonding at interface, size and shape of phases. As a result, to explain these observations researchers proposed many models to analyse the activity at the interface of crystalline-crystalline interface boundaries [11].

The proposed models in section 2.1 have left out one or more of the factors affecting the interface and thus are limited in nature and their comparison with experimental results have not always shown good alignment. One of the reasons can be the doubtful assumption made while formulating these models that equilibrium boundary conditions apply. Often it is found that the kinetics is more dominant than thermodynamics in the formation of an interfacial structure.

2.3 Amorphous-Crystalline Interfaces

The discussion about amorphous-crystalline interfaces is derived from the study of liquid/solid interfaces [22-23]. Monte Carlo simulations models have been developed to model random events at the liquid/solid interfaces. These simulations can approximate density calculation and structure by observing positions of atoms at the interfaces at distances of the order of few monolayers on either side.

Jackson [23] gave a theory based on the nearest neighbour bond model which assumes the presence of extra molecules to be randomly arranged on a crystal surface. It was also shown that the change in free energy on adding molecules to a fraction of possible sites on the surface can be related to the dimensionless entropy of crystallization. Faceting and non-faceting could be predicted for atomically smooth and rough surfaces using Jackson's model. A parameter is introduced called the Jackson's α parameter given by the formula below valid for solid/liquid interfaces at equilibrium melting temperature T_m.

$$\alpha = \left(\frac{\Delta H_m}{k_B T_m}\right)\left(\frac{z_1}{z}\right)$$

Where, ΔH_m is the heat of melting, k_B is the Boltzmann's constant, T_m is the bulk melting temperature, z is the number of nearest neighbours in the solid, z_1 is the lateral coordination number of an atom within a layer parallel to the surface layer. The first term in the α parameter is the thermodynamic factor and the second term is the geometric factor.

When $\alpha < 2$, we have a rough interface as solid liquid phases are completely mixed. When $\alpha >> 2$, we get a smooth interface with very few defects. The transition from smooth to rough occurs when $\alpha \cong 2$.

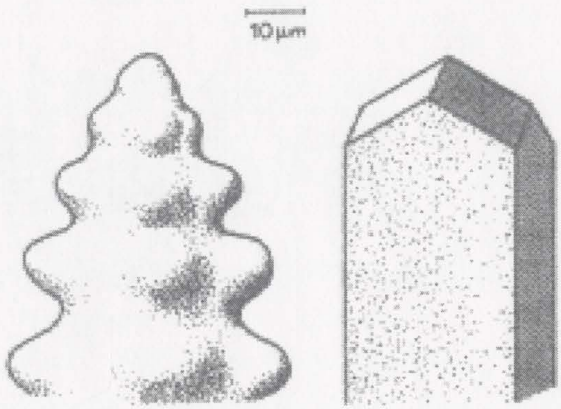

(a) (b)

Figure 2.6: Schematic depicting possible growth patterns in crystals: (a) showing non-faceted growth, (b) showing faceted growth in crystals [11].

Crystals near T_m with $\alpha < 2$ can grow by random atomic attachment to a rough interface, whereas those with $\alpha > 2$ should grow by nucleation and propagation of islands on low-indexed facet planes (see figure 2.6). The derivations made on the basis of this model are approximate due to nearest-neighbour limitation of the model, but it has been reasonable indicator between isotropic and faceted growth corresponding to rough and smooth solid/liquid interfaces.

Interfacial kinetics is described by Cahn [22] in qualitative terms by introducing the concept of "diffuse interface". Interfaces are either sharp (smooth) or diffuse (rough) so that due to inter-diffusion the transition from solid to liquid takes place over a number of atomic layers and the thermodynamic properties vary continuously across the interfacial zone [22, 24].

In relation to the orientation dependence on interfacial energy, it has been known for liquid/solid fcc metal systems that (111) or (100) planes when parallel to the interface have somewhat lower energy than interfaces having other crystal orientations.

For liquid/solid cubic metal systems the interfacial anisotropy is as large as 20 % with the interface of low energies being the (111) and (100) close-packed planes parallel to the interface [11]. For some studies involving faceting behaviour of inclusions entrapped in a solid matrix, it is also found that the anisotropies were as high as 100 % for solid/liquid hexagonal metal systems.

Not much is known about orientation dependence on interfacial energy for amorphous-crystalline systems where the amorphous phase is solid, similar to crystalline Au on amorphous glass. For studies of thin metallic film deposition on amorphous glass, factors for orientation dependence have not been explained satisfactorily. Also, since preferred orientations can also be due to many reasons such as anisotropy in crystal nucleation,

growth rates or cusps in interfacial energy curve of substrate and overgrowth etc., it is still an unanswered question.

2.4 Epitaxial Growth

The term Epitaxy is a Greek word meaning 'arrangement on'. The original definition said that epitaxy is a phenomenon of oriented-growth between two crystals when parallelism is involved between the lattices of similar lattice spacings. The epitaxial growth depends on the misfit (f), given by:

$$f = \frac{a_s - a_f}{a_f}$$

Where, a_s and a_f are the lattice parameters for the substrate and the film respectively. It was believed earlier that lattice misfit is the only parameter for epitaxial growth; this was found not to be true as epitaxy depended on many other factors like substrate/deposit properties, etc.

For the case where a crystal grows from vapour in a single component system, the differences in interfacial energy or strain energy that can occur between the growing layer and substrate during the growth process (homoepitaxy), does not need to be considered. These parameters need to be considered when growing a material of a different phase on top of a substrate, this phenomena is called heteroepitaxy [11]. The wetting behaviour of the growing material is also as important as the presence of strain and lattice mismatch between the layers.

The four primary growth modes of an epitaxial film growing on a substrate are (see figure 2.7):

- Layer-by-layer growth or Frank-Van der Merwe (FM) growth mode.
- The island growth mode or Volmer-Weber (VW) growth mode.
- The island growth mode where island grows on top of an initial smooth layer or the Stranski-Krastanov (SK) growth mode.
- The columnar growth mode. In this growth low atomic mobility leads to the formation of highly defective atomic columns of material on substrates.

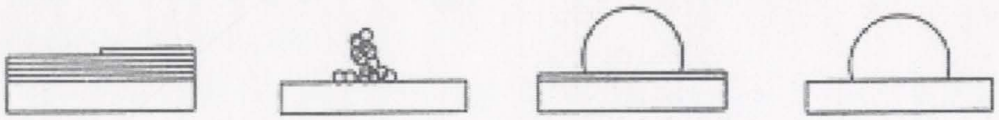

(a) (b) (c) (d)

Figure 2.7: Schematic representation of growth modes for deposition on crystalline substrate: (a) FM mode, (b) columnar growth mode, (c) SK mode and (d) VW mode [11].

The FM or ledged growth mode and columnar or continuous mode of growth results as a balance between the interfacial energy and the lattice mismatch between the layers.

2.5 Interfacial Energy

The deposition of a crystal A on a substrate crystal B, having similar crystal structure that are chemically bonded together, requires a change in energy to form an interface boundary and is given by the mathematical expression:

$$\Delta E = \gamma_A + \gamma_B - E_{AB} + E_m$$

Where, γ_A and γ_B are the surface energies of the single crystals A and B and E_{AB} is the interfacial energy [25] and E_m is the misfit energy. The equation can be modified to incorporate the charge transfer term for evaluating interfacial energy of between dissimilar materials A and B [26]. The misfit energy term E_m comes into the picture for crystals differing in lattice parameters.

An expression was derived for the study of grain boundaries, relating the interfacial energy to the misorientation or rotation angle between the boundary plane and mean [100] direction for two grains in an isotropic simple cubic material. This helps in making the plot between the interfacial energy and misorientation. The plot has cusps or local minima in interfacial energies for some particular misorientation values corresponding to orientation relationships with good lattice match. The relationship of the low interfacial energy corresponding to surface tension for grain boundaries is also very important [27]. The excess surface free energy is responsible for the shape of metal particles deposited on the surface of a substrate.

2.6 Thermodynamics of Surfaces and Interfaces

Surface processes at the interface are important in understanding interfacial phenomena. Thermodynamic relationships provide an interesting correlation between macroscopic and atomistic views of surface processes. Thermodynamically the surface tension can be viewed in terms of surface free energy or Gibbs free energy per unit volume. Thus, entropy comes into the picture and the surface tension (reversible work) is determined by the change in surface free energy of new surface formed. The surface free energy (γ), surface entropy (S) and the temperature are related by the formula:

$$S = -\left(\frac{\partial \gamma}{\partial T}\right)$$

The shape taken by the overgrowth on the substrate will be determined by minimizing the surface free energy. The resulting shape is called the equilibrium shape. The equilibrium shape is determined by Wulff construction which is a plot between the surface free energy and the anisotropy giving us an idea as to why faceting occurs in various systems. The Wulff construction has been discussed before and it appears that we can determine the equilibrium shape of overgrowth or crystal by the surface energy consideration. In the case when the surface tension is the same for all surface orientations the equilibrium shape will be a sphere as for that shape the surface energy is the minimum. But since, in reality the surface free energy varies with orientation, thus the equilibrium shape will be one that minimizes the surface free energy and will tend to enlarge the surface area of those surfaces orientations which have lower surface tensions and decrease the area of

those surface orientations which have higher surface tensions. This is the reason for faceting in crystal overgrowths.

The Gibbs free energy equation can be used to describe equilibrium at the surfaces and at interfaces:

$$\Delta G = \Delta H - T\Delta S$$

$$\Delta G = E + V\Delta P - T\Delta S$$

Where, ΔG is the change in Gibbs free energy at the interface, ΔH is the change in enthalpy at the interface, ΔS is the change in entropy at the interface, ΔP is the change in pressure, E is the internal energy, V is the volume and T is the temperature at the interfacial boundary.

At a constant pressure and an assumption that small volume change is accommodated by lattice matching across the interface boundary the equation reduces to:

$$\Delta G = E - T\Delta S$$

For Ag/Ag boundaries in sphere-rotation experiments [28], interfacial energy versus misorientation curves were plotted with variation in pressure and it was observed that the

curve shifts upwards with increase in pressure. The number of cusps decreased and the width of the cusps decreased.

Similar experiments were done with Cu/Cu sphere-plate samples [29], it was found that the curve shifts downwards as the temperature was increased. The orientation relationships corresponding to the low energy grain boundaries are affected by the entropy of vibration.

A study done on pure silver and silver alloys with and without segregation [31] shows that the entropy of mixing due to solute segregation decreases the interfacial energy and also removes some cusps in the interfacial energy versus misorientation curve.

The total entropy (ΔS_{total}) of an interfacial boundary is given by the contributions from mixing (ΔS_{mixing}), vibration ($\Delta S_{vibration}$) and configuration ($\Delta S_{configuration}$).

$$\Delta S_{total} = \Delta S_{mixing} + \Delta S_{vibration} + \Delta S_{configuration}$$

2.7 Experimental Problem Formulation

Now before we move on to the Chapter 3, Experimental, we decide the problem to work upon with some background study to it.

The systems chosen for study in this thesis are $Au/SiO_2/Si(100)$; $Au/SiO_2/Si(111)$ and Au/SiO_2. These systems are examples of crystalline/amorphous/crystalline and crystalline/amorphous systems. The reasons for orientation and growth of metal on a crystalline, non-metal with an interlayer or on an amorphous non-metal are still not fully understood.

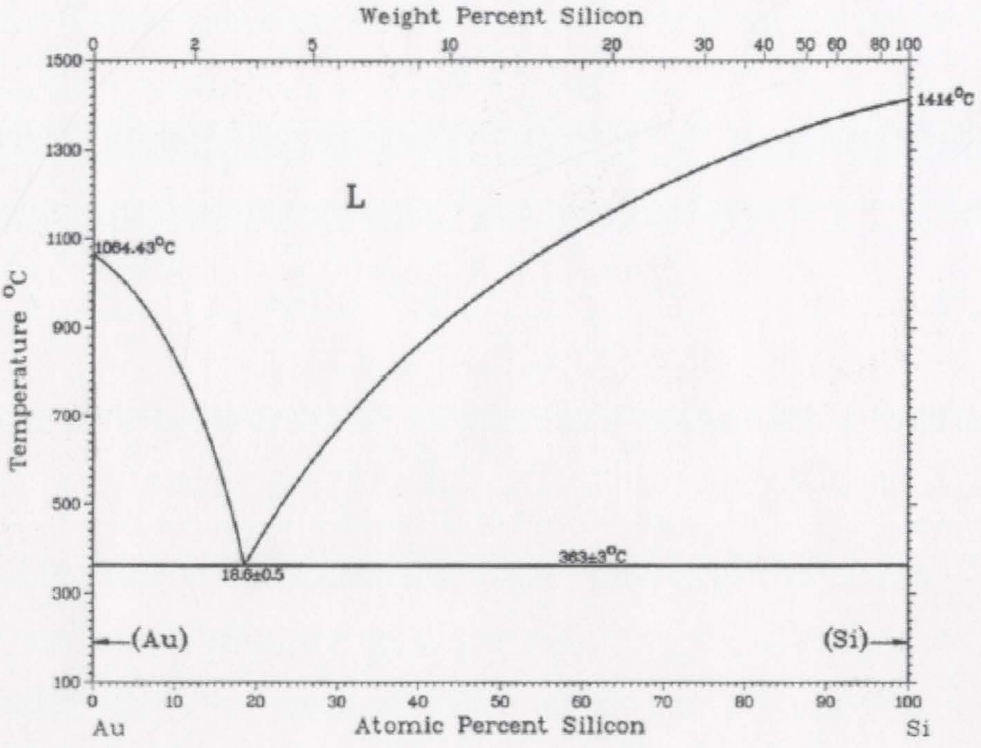

Figure 2.8: Au-Si phase diagram.

From the literature it is evident that there is an epitaxial growth of crystalline metal on a crystalline non-metal with an amorphous interlayer and this means that long range ordering effect is there which causes the metal to settle in preferred orientation. The growth of crystalline metal on the amorphous substrate is also following the same pattern except that it is not having growth in epitaxial direction. The reasons for such behaviour are owed to the concept of cusps in interfacial energy versus misorientation curve, and we will strengthen that theory in this thesis by the facts presented from our experimental results.

The electronic effects were considered to be one of the reasons for such orientation distribution in the cases where we don't consider long-range ordering effects but determining electronic effects data, such as subsurface space charge for the non-metals to prove this premise is not feasible for many crystals and interphase boundaries. The indirect measurement of orientation of metal on non-metal substrate with amorphous interlayer is relatively easier to measure experimentally.

The Au/Si system is chosen because it has been studied extensively in the past and data from epitaxial experiments are available for comparison. The Au/Si system in a temperature range of 700°C to 1000°C will form a solid-liquid [32] mixture which upon cooling will go through the eutectic transformation. The sphere-plate samples are annealed in the above temperature range and presence of any eutectic phase after annealing the sphere-plate samples will be an indication that the amorphous oxide

interlayer had holes and thus it is quiet clear that a direct contact existed between the two crystalline phases of metal and non-metal.

Distler et al. [33] could grow epitaxial metallic thin films through amorphous interlayer of SiO_2, C, polyethylene on sodium chloride and mica substrates. Distler's work could not be reproduced by Chopra et al [34]. He could not grow epitaxial films of noble metals on crystalline substrates with amorphous interlayer and so it was questioned if the amorphous coating was uniform on the substrate since epitaxial growth can occur at regions which are bare or along ledges or cleavage steps and then spread laterally.

The experimental technique used must be free from major uncertainties and able to detect low energy boundaries or cusps in the interfacial energy versus misorientation curve. Thus the modified version of the sphere-plate technique is used to study preferred orientations of crystalline metallic phases on crystalline non-metallic phase separated by an amorphous interlayer and on amorphous substrates.

The sphere-plate technique is appropriate as it is based on the statistical average [27] of large number of individual events ($\sim 10^7$ experiments) reducing the uncertainties and eliminating possibilities of holes in the amorphous interlayers. This technique has been successfully and extensively used in the past to study low energy interfaces of crystals in direct or indirect contact with each other [29, 30].

2.8 Research & Motivation

Developing a method for synthesizing gold nanoparticles on silicon substrates, covering a large area is very important for microelectronic industry and extensive research is being carried out in this area. Synthesis of aligned nanoparticles of gold on laser-generated templates [47], involves a three step procedure: first, substrate is laser-irradiated and a periodic nanorippled structure is produced; second, thin film of gold is grown by using ion-beam sputter deposition followed by a thermal treatment which facilitates formation of self-aligned gold nanoparticles. The technique can be used in a large number of substrate/film combinations.

Low-energy electron microscopy [48] was used to show that Au deposition at around 400 °C leads to an arrangement of 3D islands at single-layer steps on Si (111). This shows that a metallic thin film breaks into irregular shaped particles during annealing.

In another research gold negative-ion implantation technique [49] is used to form a single layer of crystalline gold nanoparticles. This metal nanoparticle embedded in insulator can be used as a single electron device and shows effective Coulomb blockade at room temperature.

Metal nanoparticles (Au), in application for silicon based electron devices are formed in a thin SiO_2 layer [50]. Optical reflection properties are used to study the state of nanoparticles, i.e. particle size, distribution depth.

Interfacial adhesion between Au films on SiO_x/Si substrates [51] is found to be significantly improved by an organic dendrimer monolayer. Quantitative results were obtained by nanoscratch tests performed for dendrimer-mediated Au films; it was found that the films were twice as strong as compared to simple films. This proves improved adhesion in films due to the presence of dendrimer layer.

Thin silicon nanowires were synthesized [52] using chemical vapour deposition technique, catalyzed by gold nanoparticles deposited on silicon substrates. These nanowires grew epitaxially in <111> directions on Si (100) substrates. A critical thickness of nucleating gold films was observed below which Si nanowire synthesis was not observed. A study of dependence of the Au-Si alloy droplet size and size distribution on the starting gold film thickness and the annealing conditions was made. A modified heating sequence was used which allowed growth of nanowires with diameters less than 20 nm. This is a significant step in producing electronic devices.

Thus, we see that the application of metallic particles on SiO_2/Si substrates is increasing in the micro/nano-electronic industry, underlining the importance of research in this area. The Sphere-plate technique is one of the methods of forming nanosized particles of gold on silica/silicon substrates. The various characterization techniques used help in verifying the synthesis of nanosized gold particles on the substrates. This thesis is a step towards achieving this goal.

Chapter 3

Experimental

3.1 Introduction

The technique used to study the interface of Gold/Silica/Silicon systems is a modified version of the sphere-plate technique. It basically extends from the original sphere-plate technique [27] which was used to study metal on metal and has been successfully applied in many systems to the observation of low energy interfaces for crystals in direct contact with each other. The sphere-plate technique is based on the measurement of the statistical average of a large number (~10^7 per experiment) of individual orientation events, i.e. balls per plate sample (see figure 3.1). Thus the effect of a few possible irregularities, for example holes in the amorphous oxide layer separating the two crystalline phases [27, 35, 43], on the final results is negligible. When compared with vapour-phase epitaxy experiments where a few flaws in the system could indeed affect the final result of the orientation relationship between the overgrowth and the substrate which is more collective for the film and not a statistical average of many individual events.

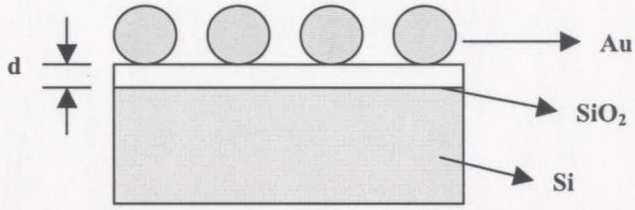

Figure 3.1: Schematic of a sphere-plate sample: Cross-section showing gold deposited on silicon with an interlayer of SiO_2 present, showing good statistics.

Upon annealing the single-crystal spheres rotate into orientation relationships which correspond to lowest interfacial energy. Thus rotation is driven by an energy change which follows the gradient in the vicinity of the cusp in the interfacial energy curve (figure 3.2).

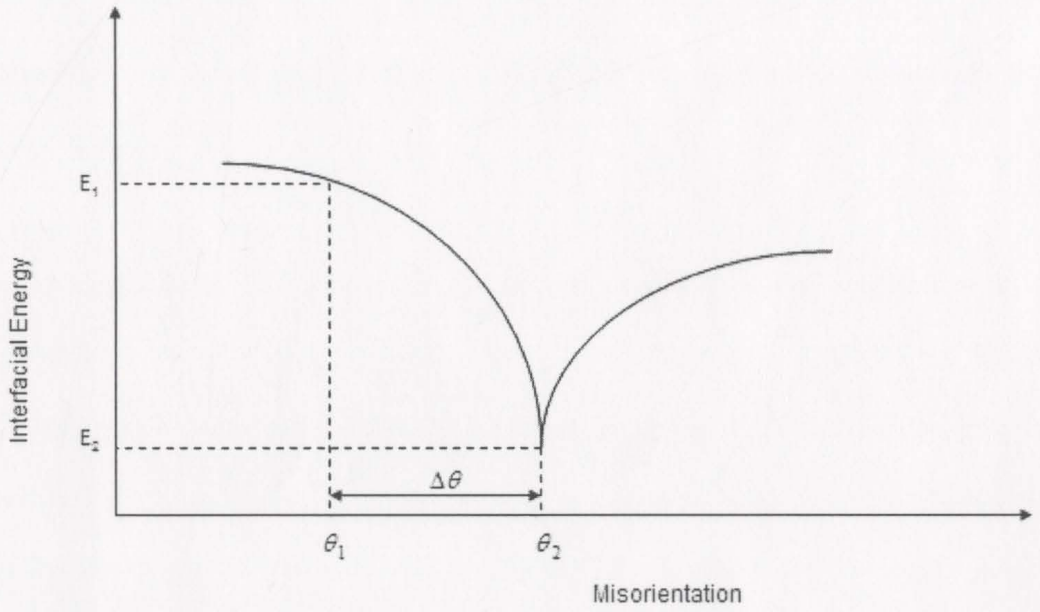

Figure 3.2: Interfacial energy vs. misorientation curve: [27].

3.2 An Account of the Sphere-Plate Technique

The original sphere-plate technique, namely version 1 was developed in 1974 [35, 43] to study grain boundaries in metals and alloys. The next version came in 1978 to eliminate the undesirable electrolytic neck removal step and was called the first modification. The version 3, also called the second modification was developed in 1982 and this is where the technique was first applied to metals on non-metal substrates. The third and final modification was made in 1986 and is called version 4 of the sphere-plate technique. This modification of the sphere-plate technique was an important step towards reducing the contamination at the interfacial region. The modified version 4 basically involves the deposition of a thin polycrystalline film of the sphere material directly onto the substrate which forms the other half of the interface [35]. This process is followed by annealing the film which breaks the film into single crystalline particles which then freely rearrange themselves into lowest interfacial energy configurations by rotation of these spheres as shown in figure 3.3.

The spherical metal particles rotate themselves until they reach equilibrium or align themselves to the preferred orientations as in the substrate. It is evident from figure 3.3 that the misorientation and mismatch decreases as planes align themselves in a special configuration. The planes try to align themselves parallel to the planes on the substrate thereby achieving a lower interfacial energy by virtue of its being into preferred orientations of low energy.

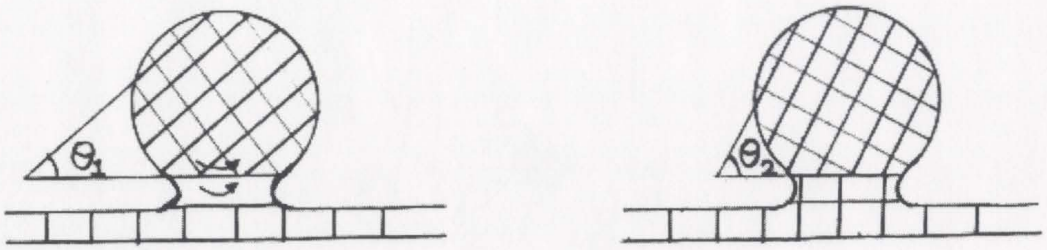

(a) (b)

Figure 3.3: Sphere rotation of balls due to annealing: Rotation occurs from (a) Intermediate anneal stage (stage II), to reach (b) High temperature anneal stage (stage III), with minimum interfacial energy. Angles θ_1 and θ_2 correspond to the misorientation values at the two stages as seen in figure 3.2.

There are three stages of film evolution; thin film deposition, film breaking into islands during the intermediate anneal stage and finally rotating into balls after the high temperature anneal stage (figure 3.4).

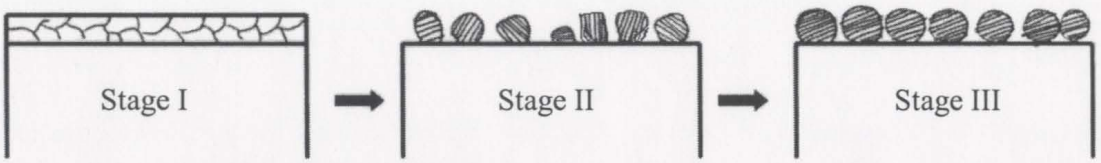

Figure 3.4: Stages of single crystal sphere formation by sphere-plate technique: Stage I, as-evaporated film; Stage II, intermediate anneal stage; Stage III, high temperature anneal stage.

3.3 Substrates Used

The substrates used were Silica glass (SiO_2) and Silicon (Si), both are non-metallic in nature. The glass substrate is amorphous and Silicon substrates are crystalline. Amorphous SiO_2 disks 2.5 mm x 1.0 mm were obtained from Esco Products Co. Inc (figure 3.5)

.

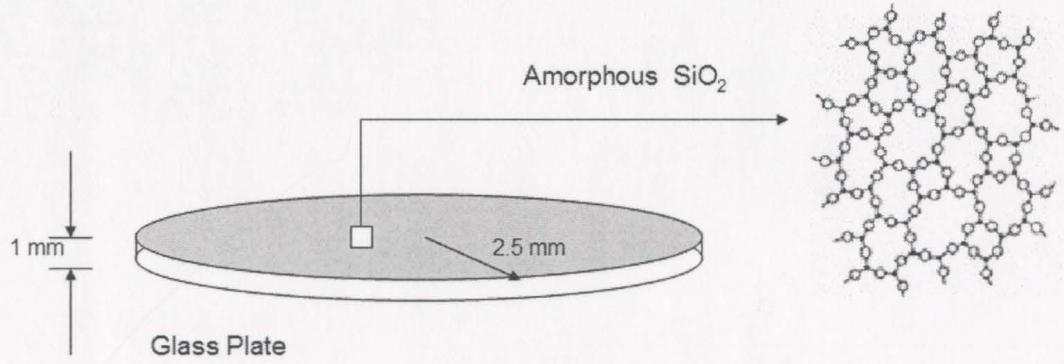

Figure 3.5: Schematic of glass substrate used: Showing dimensions and structure of amorphous SiO_2 having short range order.

The semiconductor substrates, Si(100) and Si(111) used were obtained by a substrate supplier and were supplied by the website www.universitywafer.com and Motorola. The Si(100) and Si(111) were offset by $\pm 0.5^{o}$ in orientation with the normal to the plane; with an equilibrium layer thickness of SiO_2 of 20-30 Å and 30-40 Å respectively [37]. This oxide layer is called the native oxide layer and is formed due to atmospheric oxidation. A

diamond scribe was used to cut the Si(100) and Si(111) wafers along <100> and <111> directions respectively, as shown in Figure 3.6.

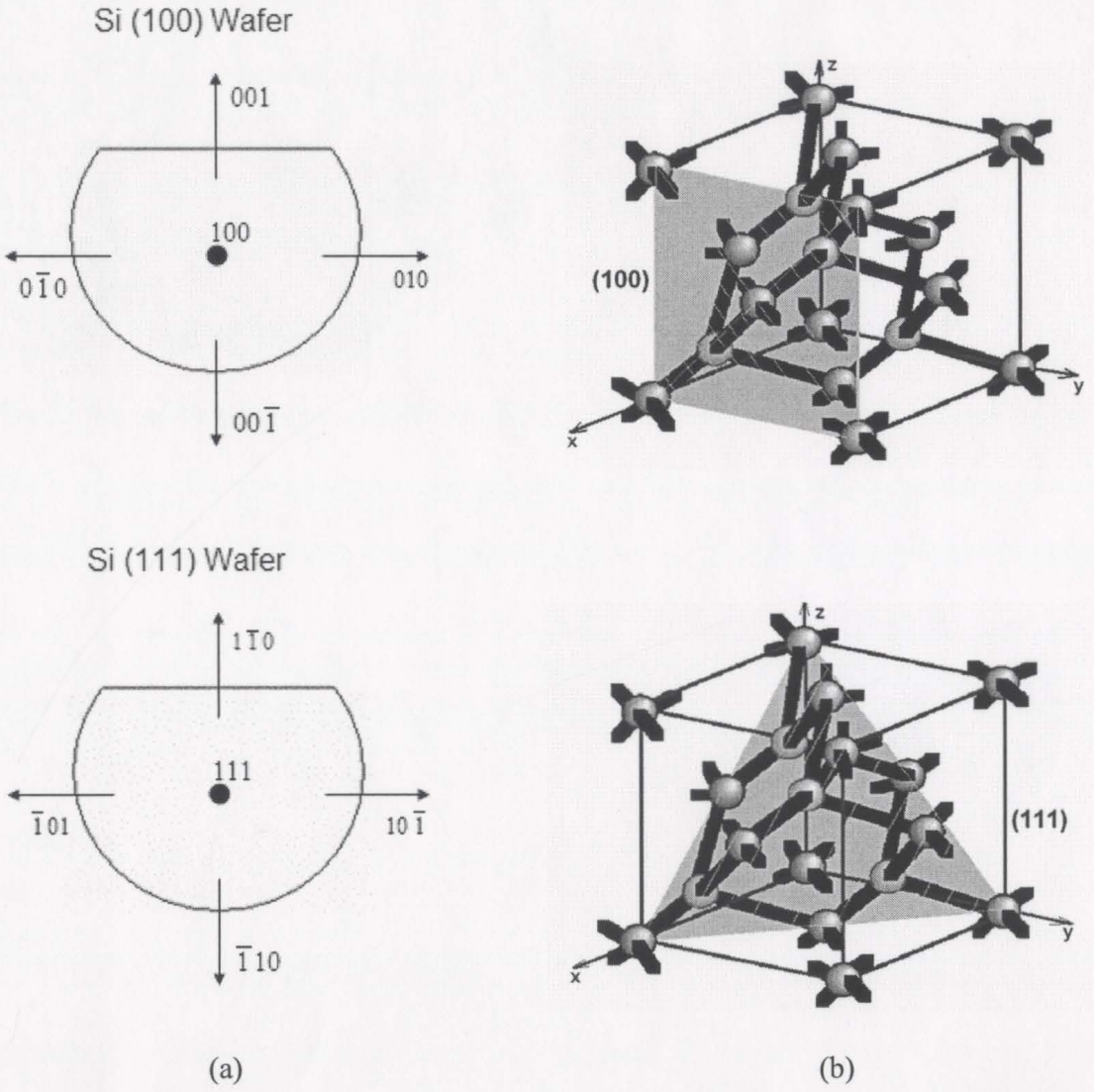

Figure 3.6: Schematic of Si(100) and Si(111) showing directions and orientation of planes on the wafer: (a) Orientation of planes in Si(100) and Si(111) wafer used as

substrates, (b) The unit cell of Silicon having diamond a structure is shown with the corresponding planes shaded.

A ±5° offset was a product specification but we also know from the literature that this forms ledges and steps enhancing epitaxial growth.

3.4 Experimental Procedure

3.4.1. Substrate Cleaning

This is one of the most important steps in the version 4 of the sphere-plate technique which we are incorporating to study the interface between the metal (Gold) and non-metal (SiO_2/Si(111)/Si(100)). The unwanted deposits on the substrate can affect the film growth, orientation and adhesion. The cleaning technique depends on the nature of substrate chosen, contaminants present and the degree of cleanliness required. Residues, fingerprints, oil, lint, dust and other airborne particles are the commonly encountered contaminants.

The substrate cleaning procedure requires the bonds between the contaminants and the substrate to be broken. These bonding forces between the substrate and contaminants are generally weak forces and thus may be broken by cleaning in detergent solution, by chemical means as in solvent cleaning or by providing enough energy to the impurities to vaporize them (i.e. by heating or particle bombardment). Etching a few layers of the

surface molecules is an approach used effectively to clean a surface in various applications, provided that the etch pits are not formed.

A modified cleaning procedure #7059 by Corning, NY was used to clean the substrates before the Au film was deposited on it. The substrates were placed in glass holders at all times to prevent them from getting scratches and before thin film deposition they were cleaned in a clean hood using the procedure described below.

The steps in the Corning Glass modified cleaning procedure #7059, Corning, New York, carried out for the substrates SiO_2/Si(111)/Si(100) in our experimentation were:

1) 5 minutes in boiling distilled water.
2) 5 minutes in a beaker containing 25 ml boiling Acetone and its vapors condensing on a cold trap.
3) Same procedure in step 2 with Methanol.
4) Same procedure in step 2 with Propanol.

3.4.2 Thin Film Deposition

Sphere-plate samples were prepared by vapour deposition technique using a Varian Bell Jar. High-purity (99.999%) Au in wire form is put in a tungsten basket, 7 cm from the source in a vacuum of 1×10^{-5} Torr, and is deposited on the substrates SiO_2, Si(111) and Si(100) which was in a plate form. The substrates were rotated throughout the

evaporation process to ensure uniform and continuous growth of thin films without any starting texture. Au film of 0.1 μm thickness was grown at ambient temperature (298 K).

3.4.3 Annealing Sphere-Plate Samples

The next step was annealing of the as-deposited sphere-plate samples in a clean quartz glass tube furnace using inert N_2 atmosphere at ambient pressure. Intermediate annealing at 0.5-0.7 T_m (530°C) with a holding time of 1.0 hour caused the film to break and form island. The final annealing step at 920°C with a holding time of 1.0 hour was required to break up the film further into spheres and rotate the spheres into low-energy orientation relationships as shown in figure 3.7.

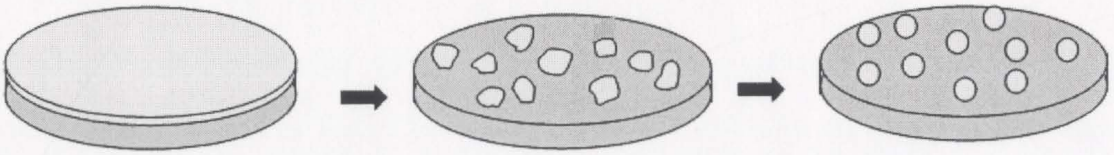

(A)

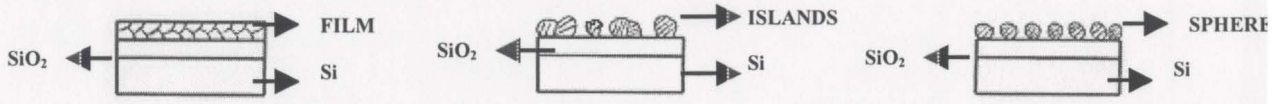

(a) (b) (c)

(B)

Figure 3.7: Schematic of the stages of film evolution on glass and silicon substrates: (a) As-deposited stage, (b) Intermediate anneal stage and (c) High temperature anneal stage for (A) Au on SiO_2, (B) Au on Si(111)/Si(100) sphere-plate samples.

The summary of the interfacial systems studied is provided in the table 3.1 shown below.

Table 3.1: Summary of experimental procedures for studied interfacial systems.

Interface Type and System	**Substrate Preparation**	**Intermediate Annealing Temperature/Holding Time**	**Final Annealing Temperature/ Holding Time**
Crystalline Amorphous Au/SiO_2	Cleaned using Corning #7059 glass cleaning method	530°C/1hr	920°C/1hr
Crystalline Amorphous Crystalline $Au/SiO_2/Si(111)$	Cleaned using Corning #7059 glass cleaning method	530°C/1hr	920°C/1hr
Crystalline Amorphous Crystalline $Au/SiO_2/Si(100)$	Cleaned using Corning #7059 glass cleaning method	530°C/1hr	920°C/1hr

In the next step once the samples were prepared they are characterized by X-ray Diffraction (XRD)-Pole Figure Determination, Scanning Electron Microscope (SEM)-Energy Dispersive Spectroscopy (EDS) and Atomic Force Microscopy (AFM). These characterization techniques are discussed in detail in the following section including details of setup and working principles.

3.5 Characterization of Sphere-Plate Samples

3.5.1 X-ray Diffraction and Pole Figure Determination

The XRD is based on the principle of path difference between two rays of a beam of X-rays. The difference between the lengths of path travelled lead to difference in phase. This phase difference is the reason behind the variation in the amplitude. The X-ray diffraction pattern of a pure substance is, therefore, like a fingerprint of the substance.

A diffracted beam is defined as a beam composed of large number of scattered rays mutually reinforcing one another (figure 3.8). Thus we see that diffraction is a scattering phenomenon of X-rays over atoms while interacting with it. The diffraction beam is a built up of the rays scattered by all the atoms of the crystal which come in the way of incident beam and the diffraction of the monochromatic X-ray takes place only at the particular angles of incidences which satisfy the Bragg's law. The phase relation determines whether we have a destructive or a constructive interference. The intensity of diffracted X-ray beam is extremely small as compared to that of the incident beam owing to the fact that most of the phase differences create a destructive interference. The peaks observed in the diffraction pattern are due to the (hkl) planes with high electron density which reflect strongly.

The Bragg's law is given by:

$$n\lambda = 2d\sin\theta$$

Where, n is the order of reflection, d is the plane spacing, λ is the wavelength and θ is the half of diffraction angle (figure 3.8). The (hkl) value of the plane is related to the'd' spacing by the lattice parameter 'a' of the unit cell.

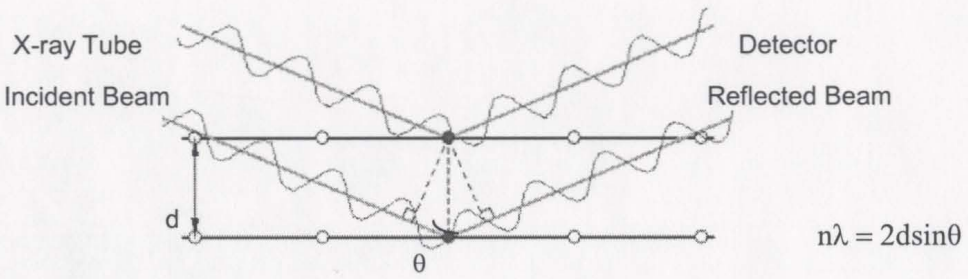

Figure 3.8: Schematic representation of diffraction of X-ray by a crystal.

The XRD instrument used for experiments was the Rigaku D/Max-2200V-PC. X-rays were generated using Cu-K_α radiation in a Cu-tube with the Cu-anode at a potential of 40 kV and current of 40 mA. The θ-2θ scans were taken for the samples for values of 2θ between 10° to 140° at a scan speed of 1°/min. The software used for the operation of θ-2θ scans was provided by Rigaku. The sampling width was 0.02° for measuring the X-ray intensity. The parameters set for the tube end are, divergence slit at 0.5° and divergence slit height at 1.2 mm. At the detector end the scatter slit was fixed at 1° and receiving slit at 0.3 mm.

The software used for search-match of chemical phase identification was purchased from Materials Data Inc. (MDI) and was called the MDI version 6.5. The search-match verifies

the Au and Si phases using the Powder Diffraction Files (PDF's). These were purchased from the Joint Committee on Powder Diffraction Standards (JCPDS), International Centre for Diffraction Data (ICDD), PA, USA, 2003.

The projection of a sphere with its pole density onto a plane is called a pole figure. An (hkl) pole figure is defined as a projection showing the density of (hkl) poles in a given direction in a sample with its pole density being directly related to its hkl integrated intensity [36]. The Schulz reflection method was used with the source and counter kept at 2θ angle for the (111) cubic metal or non-metal. The Schulz reflection method is used primarily since it is effective in exploring the central region of the pole figure which is not possible by using transmission methods.

A pole figure is scanned by measuring the diffraction intensity of a given reflection with constant 2θ at a large number of different angular orientations of a sample. A contour map of the intensity is then plotted as a function of the angular orientation of the specimen. The pole figure measurement requires a multipurpose sample holder. The pole figure measurements were made on Rigaku D/Max-2200V-PC. The data was recorded on a Personal Computer by interfacing it with the X-ray scintillator counter and using RINT2000/PC software which also plotted the pole figures in 2D. Thus, the orientation distribution of the Au particles on the substrate was measured by recording X-ray pole figures using Cu- K_α radiation for which the 2θ values for Si(111) and Au(111) are

28.442° and 38.184° respectively. The operating conditions for the generation of Cu-K_α radiation were 40 kV and 40 mA.

The values of the parameters α and δ were varied for the continuous scans using the Schulz reflection method (figure 3.9). The α angle was varied between 15° and 90° with a step size of 2° and the δ angle was varied between 0° and 360° with a step size of 2° in a coaxial scheme of scanning.

The intensity of any given reflection is proportional to the number of (hkl) planes in reflecting condition. Hence, the pole figure gives the probability of finding a given (hkl) plane normal as a function of the specimen orientation. If the crystallites in the sample have random orientation the contour map will have uniform intensity contours. X-ray intensity scans can also be plotted on a chart for particular areas of interest on the pole figure, thereby revealing the fine structure of intensity distribution.

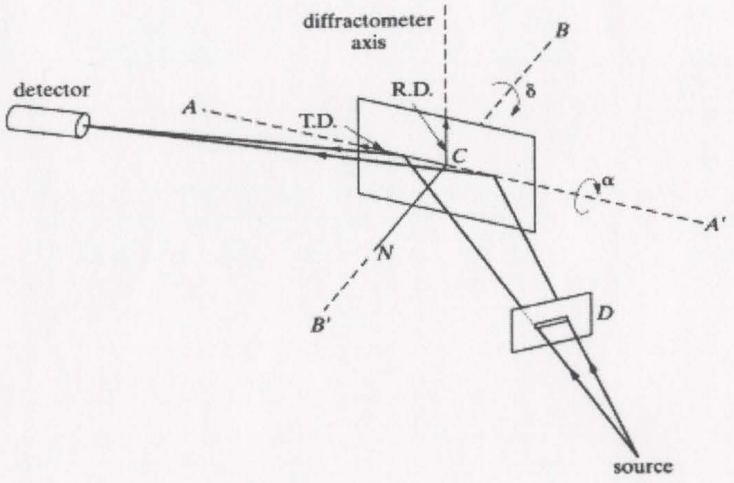

Figure 3.9: Schematic diagram of Schulz reflection method: Showing the rotational angles α, δ about the AA' and BB' axis for drawing pole figures [36].

3.5.2 Scanning Electron Microscopy and Energy Dispersive Spectroscopy

The image formed in an SEM is very different to the way it is presented to the operator because it is generated not by optical means but by secondary electron detection. The column of an SEM contains an electron gun and electromagnetic lenses. The lenses are operated in a way so as to produce a very fine electron beam, which is focused on the surface of the specimen as seen in the figure 3.10. The beam is scanned over the specimen in a series of lines and frames called a raster. The raster movement is accomplished by means of small coils of wire carrying the controlling current in the scan coils.

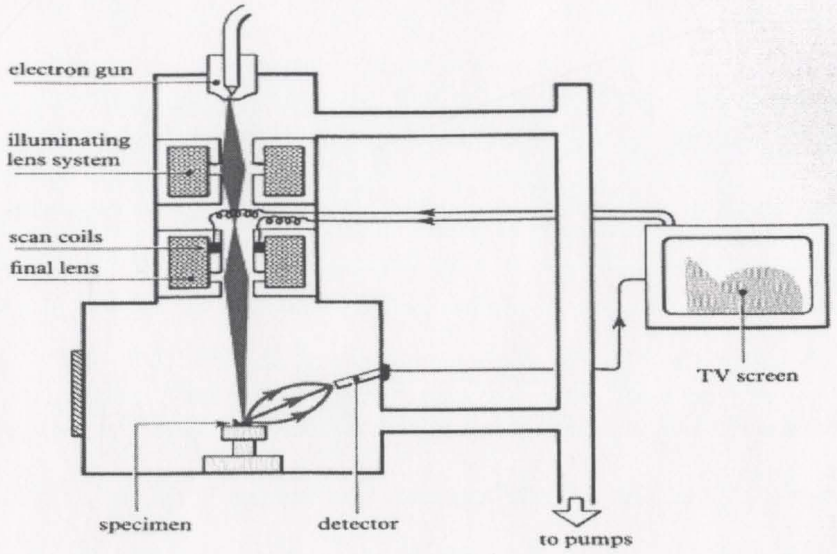

Figure 3.10: Schematic of a SEM showing its working.

The specimen is bombarded with electrons over a very small area. Several things happen to these electrons. They may be elastically reflected from the specimen, with no loss of energy. They may be absorbed by the specimen and give rise to secondary electrons of very low energy, together with X-rays. They may be absorbed and give rise to the emission of visible light, an effect known as cathodoluminescence. And they may give rise to electric currents within the specimen. All these effects can be used to produce an image. The most common method is image formation by means of the low-energy secondary electrons. This is the one we see in our SEM micrographs in the next chapter.

The secondary electrons are selectively attracted to a grid held at a low positive potential with respect to the specimen. Behind the grid is a disc held at positive voltage with respect to the specimen. The disc consists of a layer of scintillant coated with a thin layer of aluminium. The secondary electrons pass through the grid and strike the disc, causing the emission of light from the scintillant. The light is led down a light pipe to a photomultiplier tube which converts the photons of light into a voltage. The strength of this voltage depends on the number of secondary electrons that are striking the disc. Thus the secondary electrons produced from a small area of the specimen give rise to a voltage signal of a particular strength. The voltage is led out of the microscope column to an electronic console, where it is processed and amplified to generate a point of brightness on a cathode ray tube screen. An image is built up simply by scanning the electron beam across the specimen in exact synchrony with the scan of the electron beam in the cathode ray tube. The EDS analysis was done by using the data from the detection of X-rays.

The SEM used for experimentation for this thesis is the Hitachi 5570. The operating conditions are 20 kV potential at a working distance of 15 mm and 0.1 mA beam current. The samples were attached to the holder using double-sided tape. The magnification is varied to concentrate on particular spots of interest. The quality of picture obtained is the interplay between the SEM parameters such as working distance, magnification, 3D effect, contrast, spot size, etc.

In a SEM the magnification results from the ratio of the area scanned on the specimen to the area of the television and not from objective, intermediate or projector lenses to magnify the image. Increasing the magnification in an SEM is therefore achieved quite simply by scanning the electron beam over a smaller area of the specimen. The method of image formation in the SEM is similar to the ones where elastically scattered electrons, X-rays, or photons of visible light are used for image formation except that the detection systems are different in those cases. Secondary electron imaging is the most common because it can be used with almost any specimen and is less time consuming.

Energy Dispersive Spectroscopy (EDS) is an attachment on the SEM used for performing chemical analysis of the materials studied. Bombarding a specimen with electrons causes X-rays of characteristic wavelengths and energies to be emitted from the spot where the beam strikes the specimen. The EDS was carried out with an attachment to the SEM called Tracor Northern 5500 EDX. Computer analysis of the wavelength or energy spectra makes it possible to measure accurately the nature and quantity of different

elements in the material. The technique is of great value in materials science, particularly because of the range of the elements detected (Na to U), which includes the materials studied (Au, Si) and an area as small as 1 μm^2 can be analyzed with precision.

The detector in the SEM for detecting the secondary electrons was the Everhart-Thornley detector. The EDS attachment used a Si(Li) solid state detector to detect the X-rays for EDS analysis of samples.

Since the output from the SEM is a train of voltages, the operator can exert considerable control over the character of the image. Focus, magnification, brightness and contrast can all be controlled just by turning knobs on the console. In addition, the specimen can usually be tilted and rotated so that it can be examined from a wide range of viewpoints. The output from the microscope can be computer processed so that successive frames are combined and averaged, producing a striking reduction in random noise levels.

3.5.3 Atomic Force Microscopy

The Atomic Force Microscope (AFM) is one of the many types of scanned-proximity probe microscopes that work by measuring local properties, such as size, height, optical absorption, magnetism etc. with a probe or "tip" placed very close to the sample. The small probe-sample separation of the order of the instrument's resolution makes it possible to take measurements over a small area. AFM uses a sharp, micro-machined cantilever that is placed in light contact with the sample and rides along the sample as it scans it. To acquire an image the microscope raster scans the cantilever over the sample, measuring the desired local property. The raster scan operates in three modes, namely, the contact mode, non-contact mode and tapping mode. The critical components that affect sensitivity and precision of AFM are the scanner, cantilever detector and control system. Feedback obtained from the control system is crucial in analysis of data.

For this thesis we used an AFM to characterize our samples (in tapping mode) and the name of the instrument used was MFP-3D Atomic Force Microscope, Asylum Research, California, schematic shown in figure 3.11; Cantilever of silicon, "Olympus AC160TS", resonant frequency ~300 kHz. For this tip the potential maintained for the drive of the oscillation of the cantilever was 140 mV at a frequency of 305 KHz and at a scan rate of 1 Hz. The AFM used had a Nanopositioning System (NPS) [40], which allows the MF-

3D controller to maintain good control over the x-y position while operating in a closed loop.

Scanned-probe systems do not use lenses, so the size of the probe rather than diffraction effects generally limits their resolution. The probe or the cantilever sensor used in the MFP-3D is an optical lever. Optical interference can occur between the laser light reflected off the cantilever and the reflected laser off the sample. This can be reduced by improving diffraction in optics and using a low coherence light source. This can eliminate interference and provide a sensitive optical lever detection method. The noise in the optical lever detector determines the smallest forces between the cantilever and the sample that can be measured.

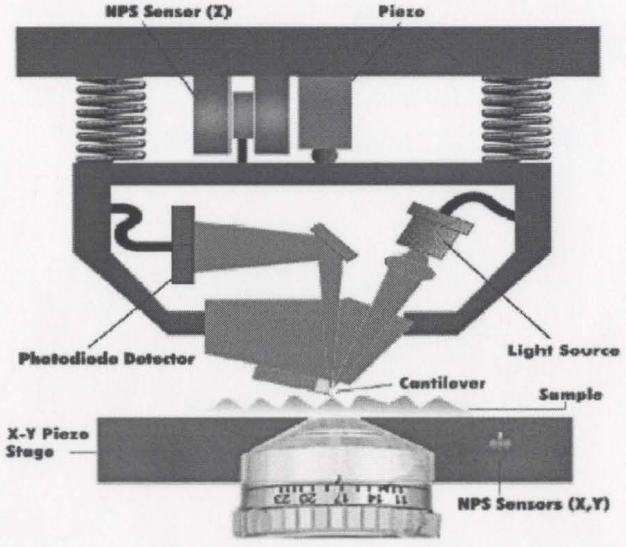

MFP-3D NPS System

Figure 3.11: Schematic of working model of an AFM: The instrument's name is MFP-3D AFM, Asylum Research, California [40]. This system had a side-on optical camera attached to it.

The AFM used in this thesis was operated in the tapping mode. Tapping mode AFM operates by scanning a tip attached to the end of an oscillating cantilever across the sample surface. The cantilever oscillates at or near its resonance frequency with amplitude ranging typically from 20nm to 100nm [41]. The tip lightly taps the sample surface during scanning, contacting the surface at the bottom of its swing (figure 3.12)

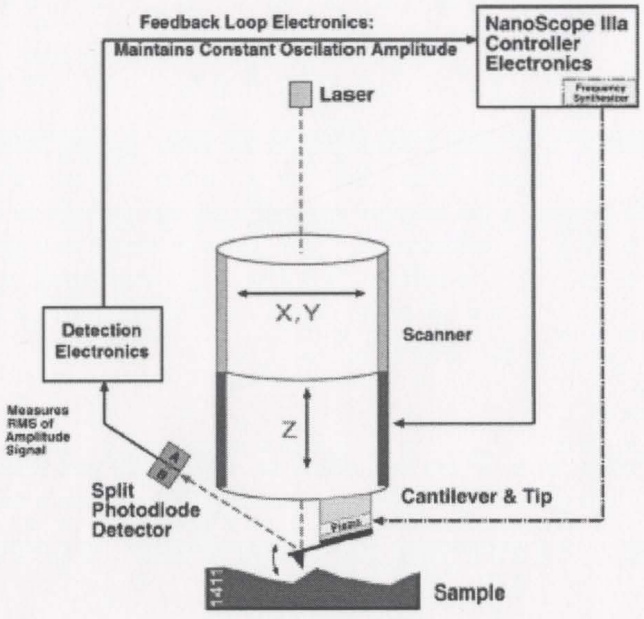

Figure 3.12: Tapping Mode AFM: [41].

A feedback loop maintains a constant cantilever oscillation by vertically moving the scanner until a set amplitude is achieved. The computer stores the vertical position of the scanner at each data point in order to form the topographic image of the sample surface. Operation can take place in ambient and liquid environments. In liquid, the oscillation need not be at the cantilever resonance. In tapping mode we can obtain a higher lateral resolution on most samples. The lateral force is lower and thus it is less damaging to soft samples imaged in air.

Laser light from a solid state diode is reflected off the back of the cantilever and collected by a position sensitive detector (PSD) consisting of two closely spaced "quadrant photodiodes" whose output signal is collected by a differential amplifier. Angular displacement of the cantilever results in one photodiode collecting more light than the other photodiode, producing an output signal, the difference between the "quadrant photodiode" signals normalized by their sum, which is proportional to the deflection of the cantilever (See figure 3.13).

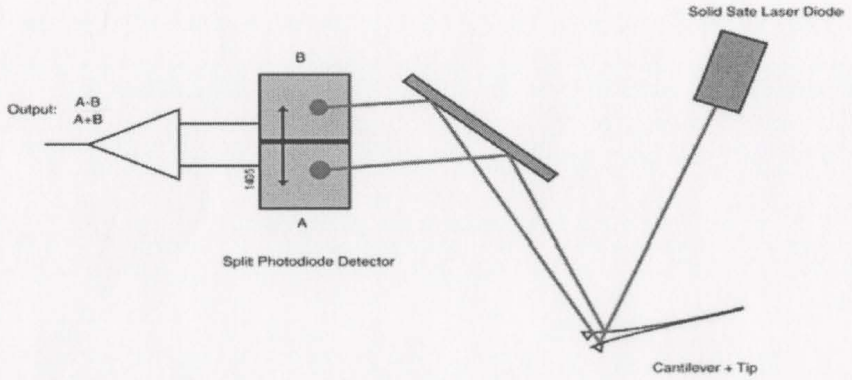

Figure 3.13: Beam Deflection in AFM: [41].

The major components of the silicon probe used are its substrate, cantilever and tip. The substrate is the body of the probe. It is the portion of the probe handled by the tweezers during installation into the cantilever holder. The cantilever is the portion of the probe that projects off of the end of the substrate. The tip mounts on the end of the cantilever. The tip is the portion of the probe that comes in proximity to the sample surface. The tip of the rectangular cantilever (Olympus AC160TS) used is tetrahedral in shape. The point of the tip has a radius of curvature < 10 nm.

One advantage of Tapping Mode AFM is an absence of lateral forces which exert torque on the cantilever. Unlike traditional contact AFM, the feedback loop keeps a vibrating cantilever at constant amplitude rather than keeping a cantilever at a constant deflection. The tip on the cantilever is modulated through mechanical excitation at its resonance. A laser beam reflects off of the microfabricated cantilever, onto a mirror, and then reflects onto a photodiode array. The laser spot oscillates vertically across the array as a result of the vibrating cantilever. The signal from the photodiodes rectifies, and then passes through a low pass filter into a DC voltage (RMS Amplitude). The magnitude of RMS amplitude is proportional to the amount of cantilever motion. The feedback system compares the RMS amplitude to the set point voltage.

For our AFM setup, the tip's relationship to the sample results in a small Z piezo movement which indicates that the cantilever is engaged with the sample surface.

There are some basic rules followed while working in tapping mode:

1) The set point voltage was always lower than the RMS voltage.

2) The difference between the RMS voltage when the tip is off the surface and the set point voltage dictates the amount of damping or "tapping force." The larger the difference, the greater the tapping force.

3) The RMS voltage controls the amount of energy that is in the cantilever. This is important to note because some samples are stickier than others. The tip may stick and hold to the sample surface if the RMS amplitude is too small. Increasing the RMS amplitude and the set point voltage may relieve this problem.

Contact mode AFM is a more traditional approach of operation. In this mode attractive or repulsive forces are measured between a tip and the sample [38]. In repulsive contact mode, the instrument lightly touches a tip at the end of a cantilever to the sample. As a raster-scan drags the tip over the sample, a detection apparatus measures the vertical deflection of the cantilever, which indicates the local sample height. Thus, in contact mode the AFM measures hard-sphere repulsion forces between the tip and sample.

In Non-contact mode, AFM derives topographic images from measurements of attractive forces; the tip does not touch the sample [39].

AFM can achieve a resolution as high as 10 pm under some special conditions, and unlike electron microscopes, can image samples under liquids.

Chapter 4

Results and Discussion

4.1 Introduction

The prepared samples of the systems mentioned previously were studied by characterizing them with XRD/Pole Figure, SEM/EDS and AFM techniques. The sphere-plate samples were obtained by annealing vapour deposited thin metal films on a substrate to study the reorientation of metal particles and examine the preferred orientations and the directional orientation. The polycrystalline thin film of Au, with annealing, breaks into islands by grain boundary grooving and is followed by spheroidization and particle coarsening (see figure 4.1).

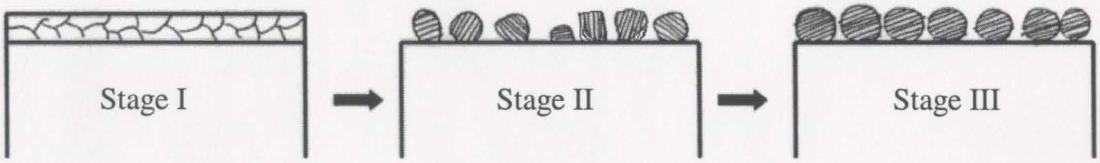

Figure 4.1: Three stages of sphere-plate technique: Stage I, as-evaporated film; Stage II, intermediate anneal stage; Stage III, high temperature anneal stage.

As seen from the figure 4.1, we see the three stages of film deposition and re-orientation. The first stage is the as-deposited polycrystalline film. In the intermediate anneal stage (530°C) we see how the film breaks into islands with Au particles of uneven shape and size. In the high temperature anneal stage (920°C), Au particles rotate into spheres and settle themselves in the more stable preferred orientation planes with (111) planes aligned parallel to the interface. As the annealing temperature is increased the Au also aligns into (222) preferred orientations. These observations were made by inspecting the peaks of intensity versus 2θ plots obtained by XRD.

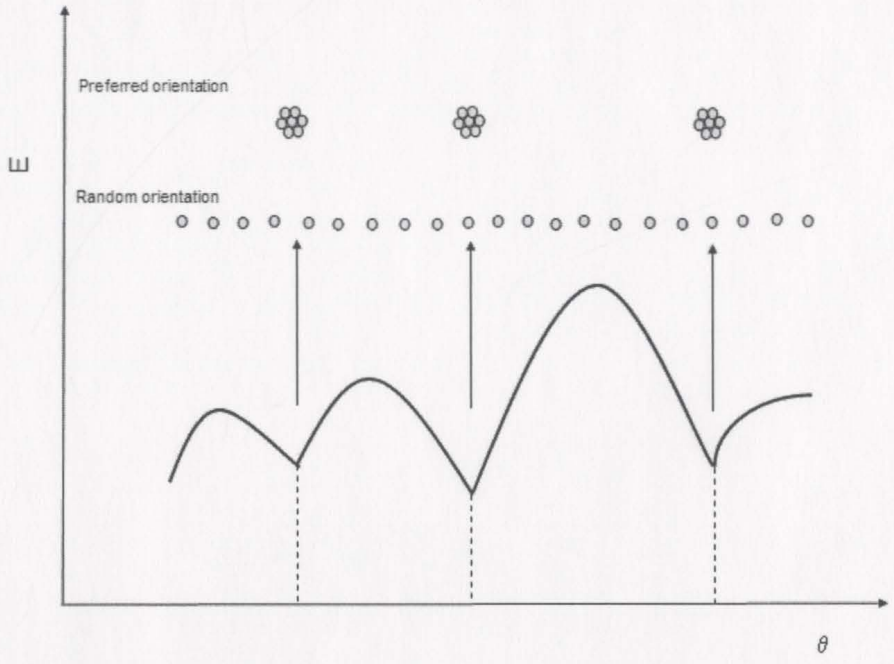

Figure 4.2: Cusps in the Interfacial Energy versus Misorientation plot: Showing random and preferred orientations of balls in stage I and stage III of the sphere-plate technique [27].

Au has, face centered cubic unit cell and Silicon has a diamond structure. The most preferred plane for Au to grow is (111) as it is the most closed packed, but in spite of this we have different planar orientations for the growth of Au particles on Silicon substrates.

4.2 XRD and Pole Figure Results

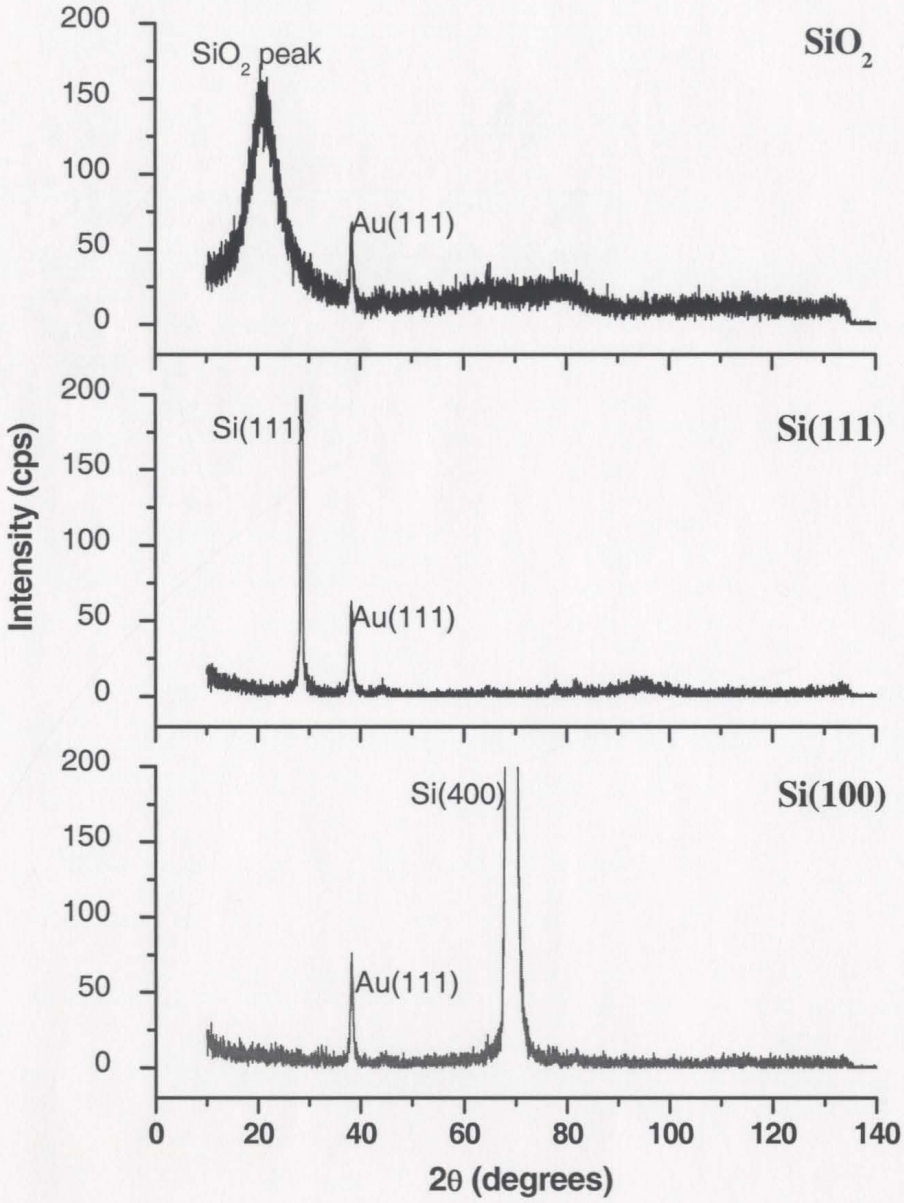

Figure 4.3: XRD patterns for stage I: As-evaporated Au on SiO_2/Si(111)/Si(100) sphere-plate samples.

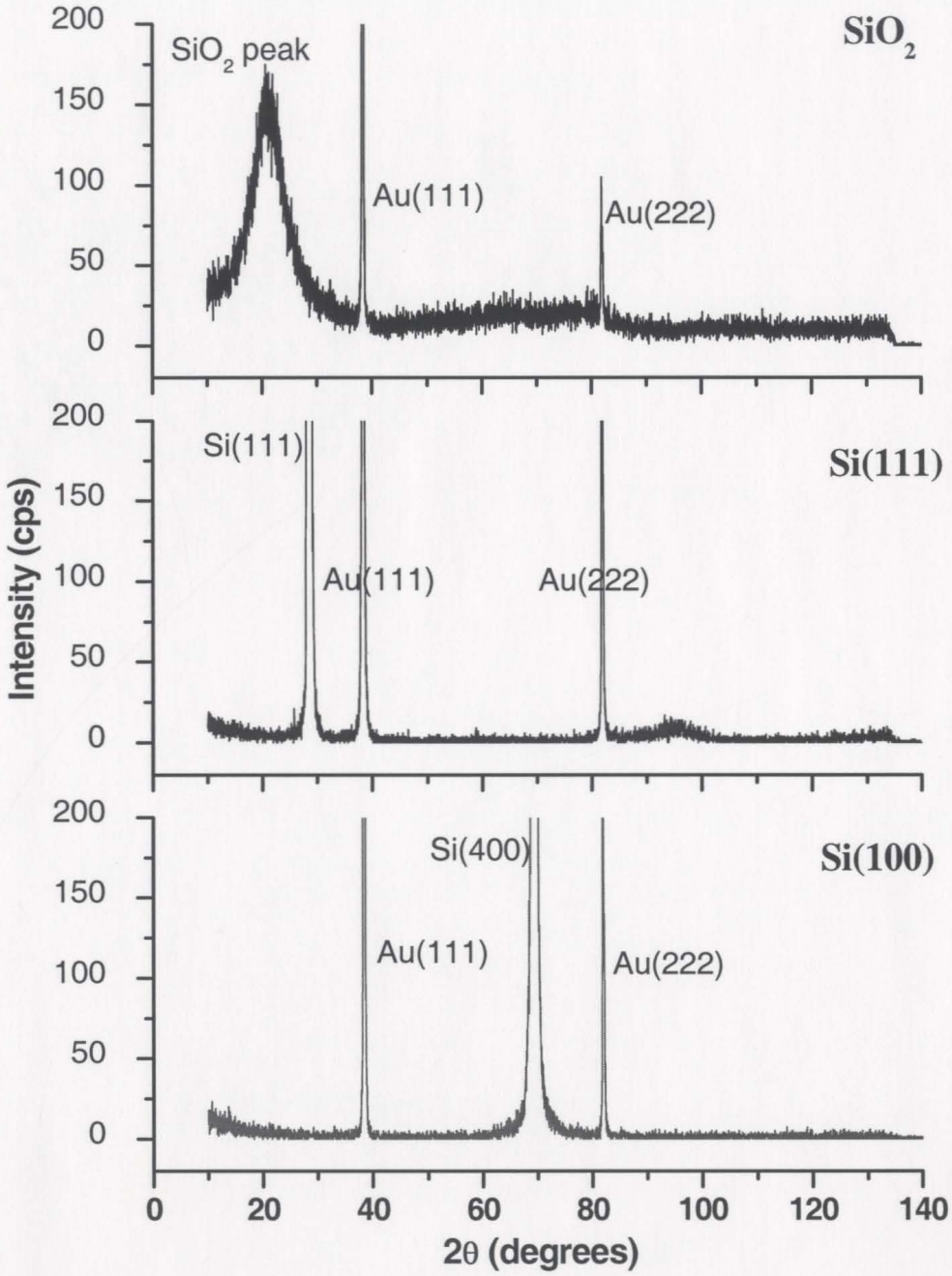

Figure 4.4: XRD patterns for stage II: Intermediate Anneal Au on SiO_2/Si(111)/Si(100) sphere-plate samples.

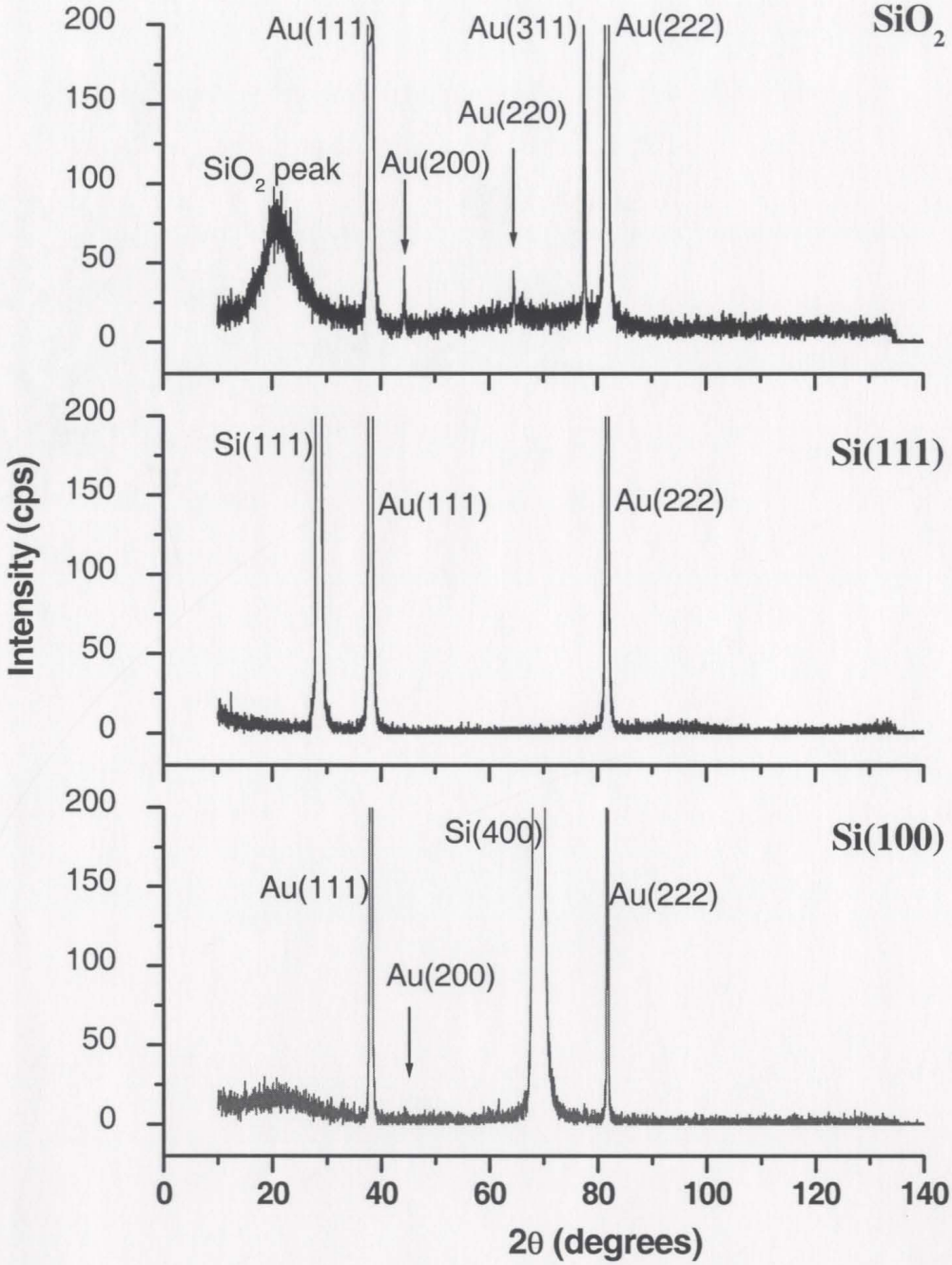

Figure 4.5: XRD patterns for stage III: High Temperature Annealed Au on SiO_2/Si(111)/Si(100) sphere-plate samples.

Comparison of figure 4.3, 4.4 and 4.5 indicates the preferred orientation planes for the three samples at three different annealing temperatures. It is very clear that Au(111) and Au(222) planes are the preferred orientations for Au on all substrates studied.

In XRD the X-ray used for characterizing the samples can penetrate up to a depth of 20 μms (figure 4.6). Thus the information contained in the reflected X-rays is also of the substrate material along with the Au deposited on it. For this reason we could observe peaks of Si(111), (222) and Si(400) in spite of an interlayer of SiO_2 in our Si substrates and also we even observed the SiO_2 peak for glass substrate.

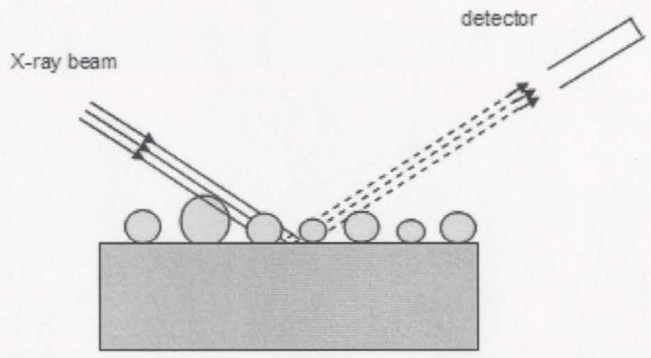

Figure 4.6: X-ray diffraction of sphere-plate samples: Schematic showing incident X-ray, sample, reflected beam and detector in characterization by XRD technique.

The tables below summarize the raw data and results from the XRD patterns in figures 4.3 to 4.5.

Table 4.1: XRD peaks data for as-evaporated stage samples: Stage I.

SiO_2 substrate		**Si(111) substrate**		**Si(100) substrate**	
Peak	**I(cps)/2θ(deg)**	**Peak**	**I(cps)/2θ(deg)**	**Peak**	**I(cps)/2θ(deg)**
SiO_2	173/20.48	Si(111)	1570/28.64	Si(400)	284655/69.16
Au(111)	68/38.48	Au(111)	63/38.26	Au(111)	76/38.24

Table 4.2: XRD peaks data for intermediate anneal stage samples: Stage II.

SiO_2 substrate		**Si(111) substrate**		**Si(100) substrate**	
Peak	**I(cps)/2θ(deg)**	**Peak**	**I(cps)/2θ(deg)**	**Peak**	**I(cps)/2θ(deg)**
SiO_2	175/20.7	Si(111)	266377/28.56	Si(400)	72331/69.3
Au(111)	1550/38.38	Au(111)	4666/38.34	Au(111)	1695/38.44
Au(222)	105/81.82	Au(222)	382/81.84	Au(222)	238/81.88

Table 4.3: XRD peaks data for high temperature anneal stage samples: Stage III.

SiO_2 substrate		**Si(111) substrate**		**Si(100) substrate**	
Peak	**I(cps)/2θ(deg)**	**Peak**	**I(cps)/2θ(deg)**	**Peak**	**I(cps)/2θ(deg)**
SiO_2	95/21.76	Si(111)	266311/28.76	Si(400)	258710/69.06
Au(111)	75373/38.14	Au(111)	24593/38.14	Au(111)	5255/38.14
Au(222)	9640/81.68	Au(222)	3591/81.66	Au(222)	325/81.68
Au(220)	40/64.56			Au(200)	8/44.38
Au(200)	48/44.38				
Au(311)	290/77.52				

The raw data helps us in concluding that as the temperature of annealing was increased we observed higher peaks of Au. The gold particles rotated themselves into preferred orientations. Different preferred planes were also observed to be showing peaks which were not visible for the as-evaporated samples.

Thus from the XRD data, we confirm the presence of gold and silicon, looking at their peaks. The peak of Au increasing in intensity and orientation with annealing temperature signifies that the Au film breaks into islands followed by its rotation into Au balls. Thus XRD was helpful in confirming the preferred orientations of the planes in the samples.

Pole figures were useful in determining the directional orientations of the samples and it was found that with increase in annealing temperature we got better directional alignment.

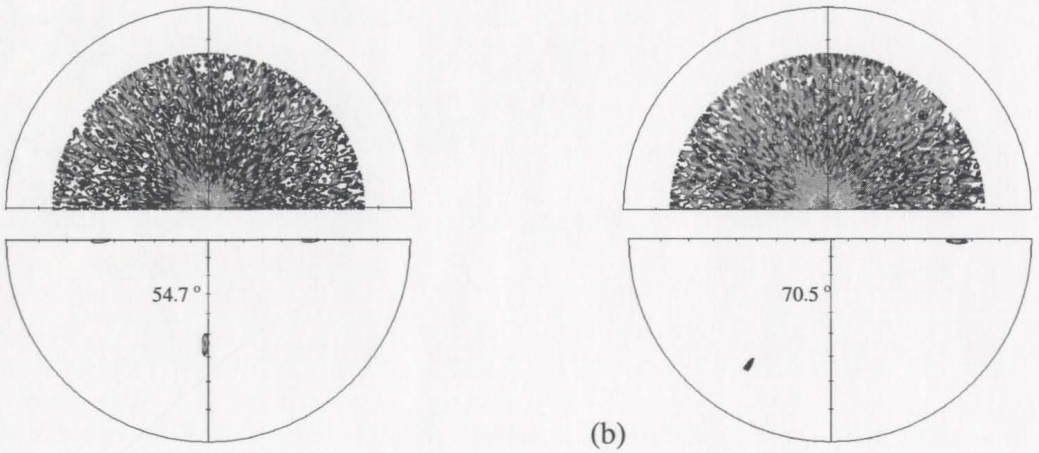

Figure 4.7: Pole figures of $Au/SiO_2/Si$ samples in the stage I.

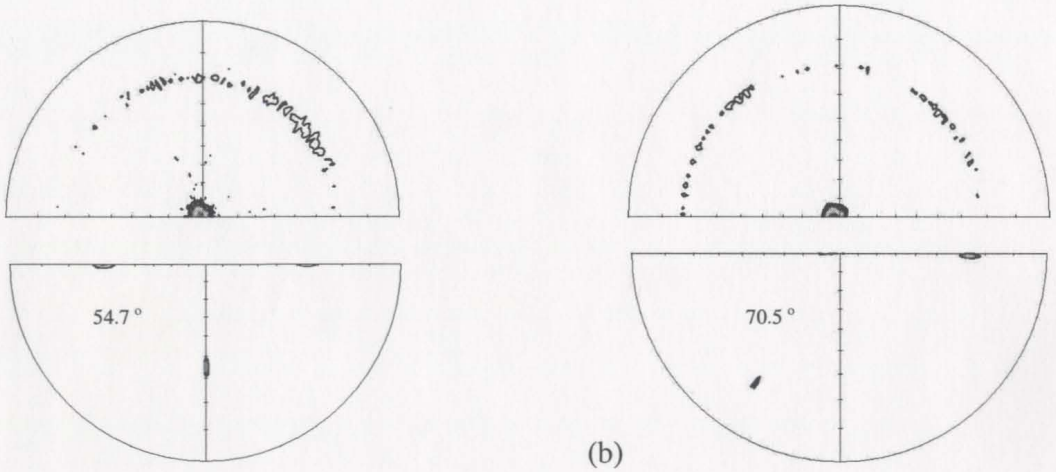

Figure 4.8: Pole figures of $Au/SiO_2/Si$ samples in the stage II.

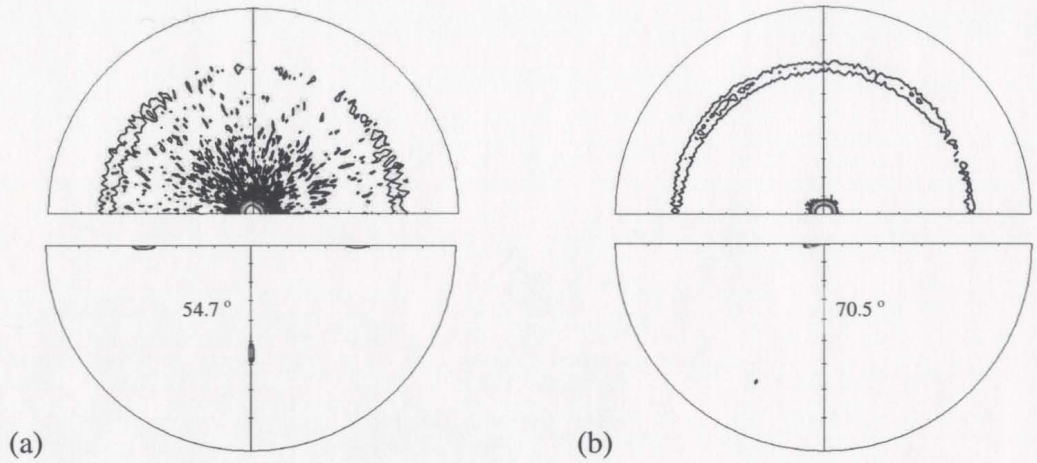

Figure 4.9: Pole figures of Au/SiO_2/Si samples in the stage III.

In the figures 4.7, 4.8 and 4.9 shown above we have, (a) Au/Si(100), (b) Au/Si(111). Where the upper part is for Au(111) poles of Au balls and lower part is for Si(100)/Si(111) poles of respective substrate.

Since the pole figures have similar pattern for both halves, we choose to show only the upper part of the pole figure for the Au(111) poles of Au and the lower portion represent the (111) poles of the substrate. All pole figures are set at 2θ = (111) plane for Au(111) poles or for Si(111) poles.

The following orientation relations were observed from the pole figure analysis for Au on Si samples:

Table 4.4: Orientation relationships for $Au/SiO_2/Si(100)$ samples: In all the three stages of sphere-plate technique.

Stages	**Planar relationships**	**Directional relationships**
As-evaporated, stage I	$(111)_{Au} \parallel (100)_{Si}$	without direction
Intermediate anneal, stage II, (530°C)	$(111)_{Au} \parallel (100)_{Si}$	without direction
	$(100)_{Au} \parallel (100)_{Si}$	without direction
High temperature anneal, stage III, (920°C)	$(111)_{Au} \parallel (100)_{Si}$	without direction
	$(100)_{Au} \parallel (100)_{Si}$	without direction
	$(100)_{Au} \parallel (100)_{Si}$	$<100>_{Au} \parallel <100>_{Si}$ "epitaxy"

Table 4.5: Orientation relationships for $Au/SiO_2/Si(111)$ samples: In all the three stages of sphere-plate technique.

Stages	**Planar relationships**	**Directional relationships**
As-evaporated, stage I	$(111)_{Au} \parallel (111)_{Si}$	without direction
Intermediate anneal, stage II (530°C)	$(111)_{Au} \parallel (111)_{Si}$	without direction
	$(111)_{Au} \parallel (111)_{Si}$	$<111>_{Au} \parallel <111>_{Si}$
High temperature anneal, stage III, (920°C)	$(111)_{Au} \parallel (111)_{Si}$	without direction
	$(100)_{Au} \parallel (100)_{Si}$	$<111>_{Au} \parallel <111>_{Si}$ "epitaxy"

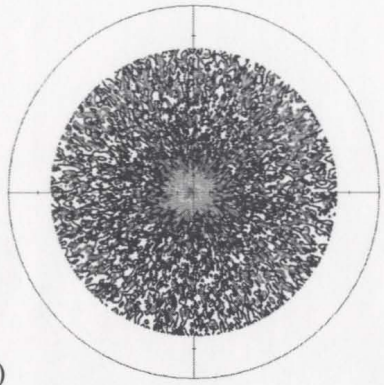

(a)

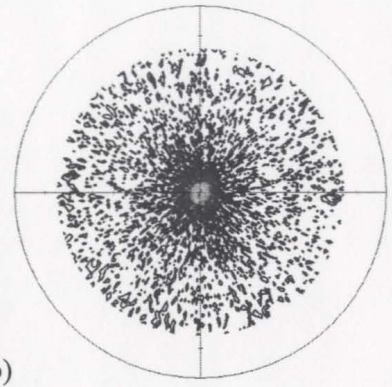

(b)

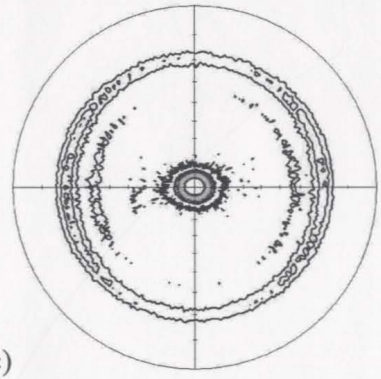

(c)

Figure 4.10: Pole figures of Au/SiO_2 samples for all stages: (a) As-evaporate sample, stage I, (b) Intermediate anneal sample, stage II (c) High temperature anneal sample, stage III.

The images of pole figure in figure 4.10 for Au(111) poles on SiO_2 glass is different than the pole figures for Au on Si(figure 4.7 to 4.9), where Si had a separate pole figure for the bottom half, as we do not have a separate pole figure for the substrate glass. This is because substrate glass is amorphous and the pole figure for it will be blank as no poles exist.

The following orientation relations were observed from the pole figure analysis for Au on SiO_2 samples:

Table 4.6: Orientation relationships for Au/SiO_2 samples: In all the three stages of sphere-plate technique.

Stages	**Planar relationships**	**Directional relationships**
As-evaporated, stage I	$(111)_{Au}$ || Amorphous SiO_2	without direction
Intermediate anneal, stage II (530°C)	$(111)_{Au}$ || Amorphous SiO_2	without direction
High temperature anneal, stage III, (920°C)	$(111)_{Au}$ || Amorphous SiO_2	without direction

Observation of pole figures suggests that the X-ray intensity of the poles increases with annealing temperature which corresponds to an increasing number of planes aligning into these preferred orientations. The orientations also correspond to cusps in the interfacial energy curve which form interfaces of low interfacial energy. The higher the X-ray intensity the more preferred are the orientations. One of the preferred orientations for the systems of Au on Si substrates is epitaxial (see "epitaxy" in table 4.4 and 4.5).

These orientation relationships for {111} metal close packed planes were also reported to be present in previously studied fcc metal/SiO_2 and Ag/Si interface systems by X-ray methods [42-43].

Orientations for (200) metal close packed planes have also been reported in Ag/Si and Au/Si interface systems by X-ray methods [43] and cross-sectional transmission electron microscopy [32, 44-46].

We observed that the as-evaporated polycrystalline film of Au is having an orientation relationship with the crystalline substrate through an amorphous interlayer, confirming that epitaxial growth occurs through the amorphous interlayer as in the literature.

4.3 SEM Results

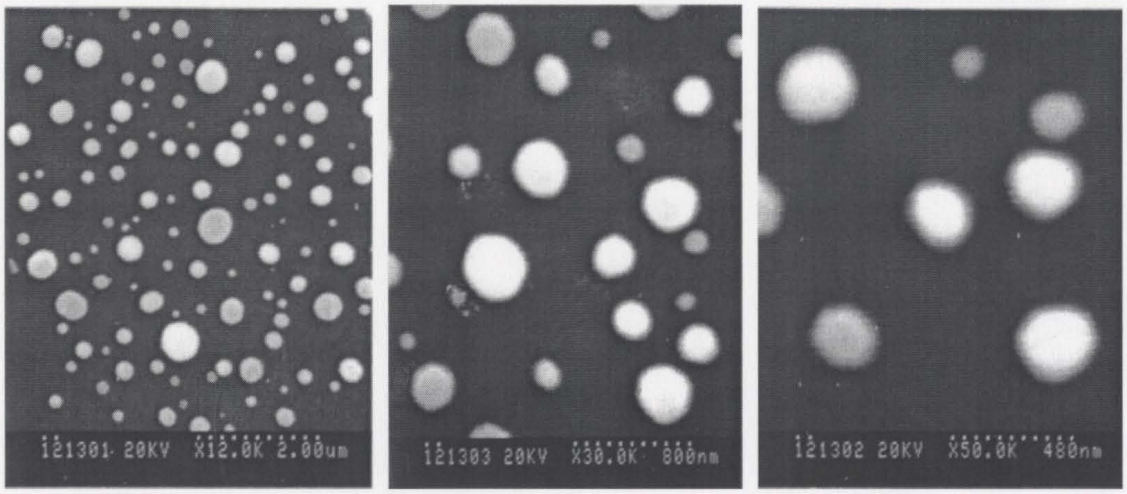

(a) (b) (c)

Figure 4.11: SEM micrographs of $Au/SiO_2/Si(111)$ samples after stage III: The magnifications are (a) 12,000 X, (b) 30,000 X and (c) 50,000 X respectively.

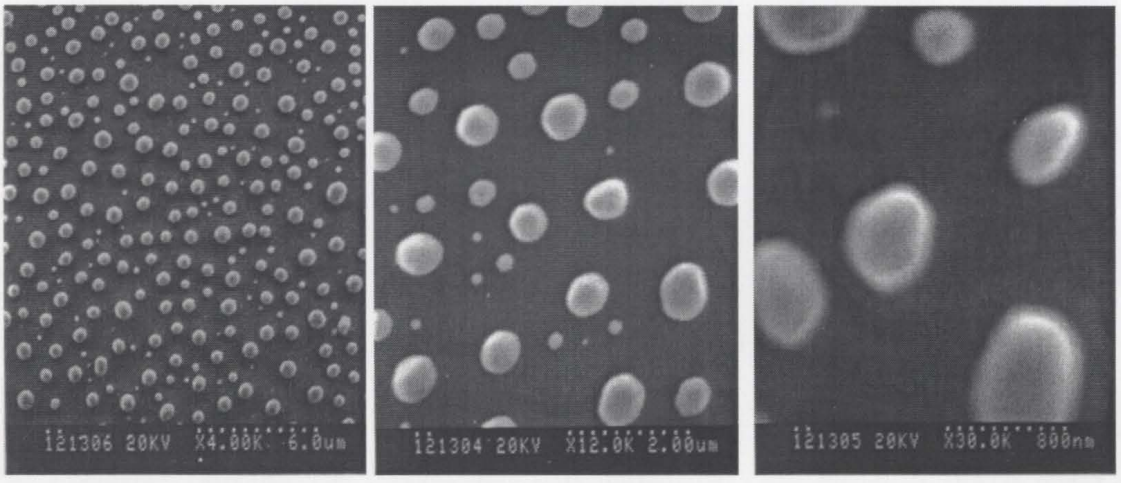

(a) (b) (c)

Figure 4.12: SEM micrographs of $Au/SiO_2/Si(100)$ samples after stage III: The magnifications are (a) 4,000 X, (b) 12,000 X and (c) 30,000 X respectively.

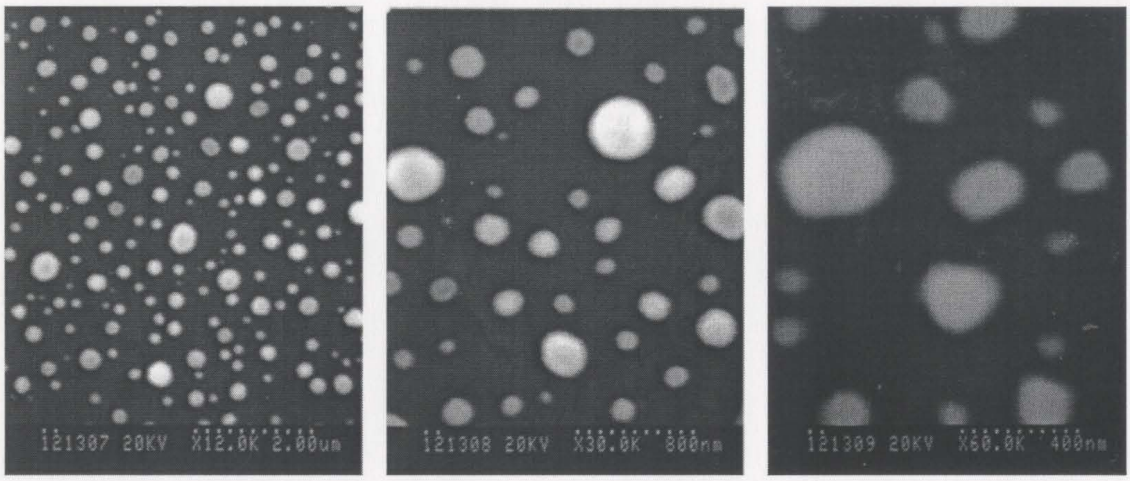

(a) (b) (c)

Figure 4.13: SEM micrographs of Au/SiO_2 samples after stage III: The magnifications are (a) 12,000 X, (b) 30,000 X and (c) 60,000 X respectively.

Looking at the SEM micrographs (see figures 4.11 to 4.13) of the stage III samples we observed spherical balls of Au, which confirms our sphere plate and particles rotating into lowest interfacial energy configuration theory.

The SEM pictures shown above are for the stage III or the high-temperature anneal stage of the three sphere-plate samples. The micrographs of as-evaporated and intermediate anneal samples were also studied and it was confirmed by observation that stage 1/as-evaporated sample showed polycrystalline grain morphology and the stage 2/intermediate anneal sample showed uneven shaped, island like Au particles. This observation combined with the spherical gold particle observation is consistent with the theory of sphere rotation and Au particles settling into minimum energy, preferred orientations.

SEM/EDS have an electron beam striking the sample (figure 4.14). This electron beam has a penetration depth. The detector detects the secondary electrons coming out of the sample up to a depth of 0.1 μms and thus the image is formed. The X-rays emitted from this volume have information between the depth of 1-2 μms. These X-rays were used for EDS analysis of the samples and thus ascertaining the elements on the sample (Au, Si).

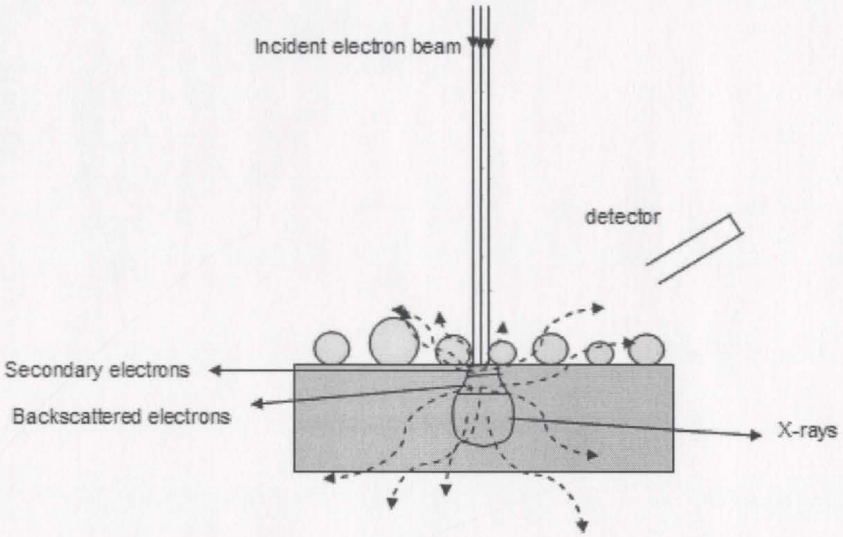

Figure 4.14: Electron beam interaction of sphere-plate sample: Schematic to show, how SEM/EDS are used to characterize samples by secondary electron imaging and X-ray analysis respectively.

The Secondary electrons for imaging were detected by Everhart-Thornley detector and X-rays for EDS analysis were detected by Si(Li) solid state detector. The SEM images gave us 3D pictures of high resolution.

On observing these SEM micrographs (figures 4.11 to 4.13) it is noted that some faceted particles of Au are present. These particles were having distortions from a perfectly spherical shape and it can be concluded that since these samples have undergone annealing the Au particles have attained a final equilibrium shape. The facets are the sides of planes which have minimum surface energy and are favourable for growth of the particle. Also from the Jackson's model we get an indication that for amorphous-crystalline interfaces we get faceting for $\alpha > 2$.

The particles of Au after sphere rotation follow a pattern as observed from the SEM. All the particles were determined to be approximately in a range of 0.05 to 1 μm; this phenomenon was consistent for all the stage III/high temperature annealed sphere-plate samples. The SEM image was studied and a sampling of the size of the balls was done. The size of approximately 100 balls was measured for all stage III sphere-plate samples and we got the following data for the size distribution. Qualitative study was done on stage III SEM micrographs to determine the particle size.

Table 4.7: Size distribution of Au particles on sphere-plate samples.

Sample Type	Maximum Size(μm)	Minimum Size(μm)	Average Size(μm)
Au/SiO_2/Si(111)	0.72	0.06	0.15
Au/SiO_2/Si(100)	0.80	0.08	0.16
Au/SiO_2	0.60	0.04	0.14

Thus we see that the average particle size is 1.5-1.6 times the thickness of the polycrystalline film. This owes to the fact that the film "breaks-up" at the grain boundaries, during the annealing process. Surface diffusion occurs during this stage and we see particles of different sizes building up on the substrate. The average size is higher than the film thickness as the breaking of film leads to empty space between islands in the intermediate anneal stage and spheres in the high-temperature anneal stage.

It was also observed that the size of Au spherical particles on the substrate Si(100) was slightly greater than the Si(111) substrate, followed by SiO_2 glass substrate. This confirms the fact that SiO_2 has a definitive effect on the size and size distribution of Au particles. The average SiO_2 interlayer thickness on Si(100) was 25 Å and on Si(111) was 35 Å [37], thus it is evident that the presence of more SiO_2 caused the average size of Au balls on Si(111) to be less than that on Si(100). This could be due to the fact that SiO_2 has amorphous structure with short-range order and thus growth of Au(111) or Au(222) is controlled differently. Also it seems that we are having long-range ordering due to crystalline Si(100) and Si(111) and this crystalline information is transmitted across the interlayer, indicating that the interface runs right through the SiO_2 interlayer otherwise it is not feasible to pass on the preferred orientation information through the amorphous interlayer.

4.4 AFM Results

The AFM instrument used to characterize the sphere-plate samples probes with a Si cantilever. This had a tip which scans the samples using raster scans and the morphology and topography of the sample surface is detected in this process. The detector is a split photodiode which detects deflection, amplitude or tip motion and Z piezo or cantilever position from the reflected laser. The AFM instrument used had a laser beam for detection purposes. The micrographs we obtained from the AFM studies report information regarding the height (nm), amplitude (nm) and phase shift (deg). This information can be interpreted from the scale that comes along with each micrograph (see figure 15); this scale can have colour contrast to distinguish between regions of different height, amplitudes and phase shifts.

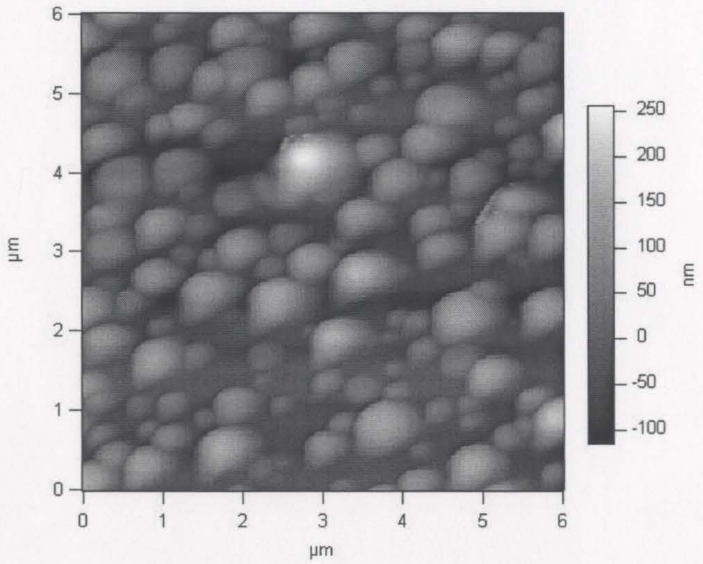

(a)

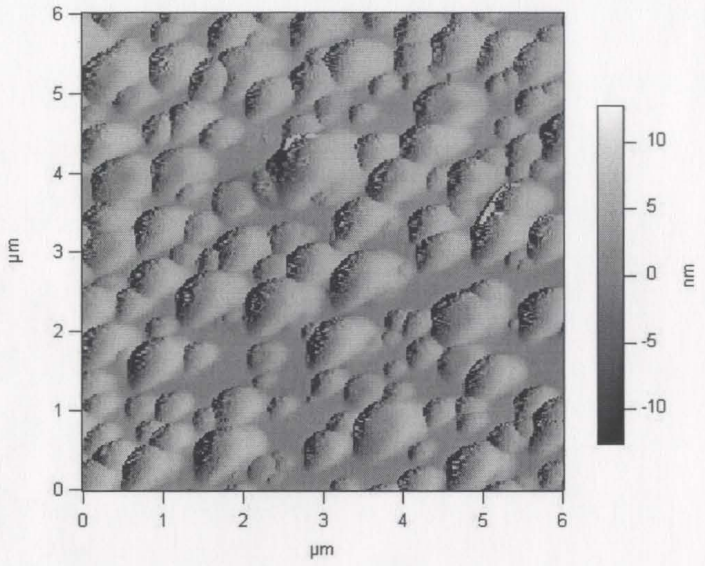

(b)

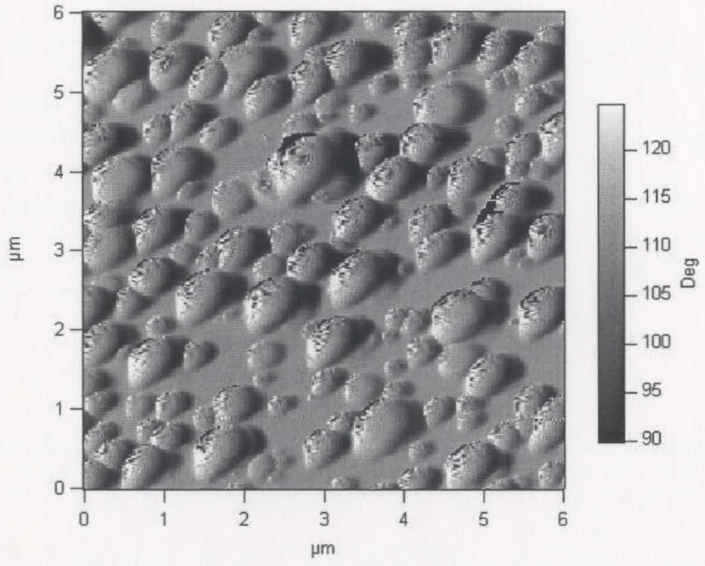

(c)

Figure 4.15: AFM micrographs for stage III, $Au/SiO_2/Si(100)$ sample: showing (a) height (nm), (b) amplitude (nm) and (c) phase (deg).

The height resolution has good precision but the lateral resolution along the width is not very accurate. The trace observed on the micrograph can be explained as the convolution of the tip with sample topography. The tip may pick up particles which will then change its shape. The height micrograph (figure 4.15) gives the height, amplitude micrograph tells us the error and the phase micrograph or the phase shift gives us the phase image. The error or the noise is comparable to the derivative of the height image.

The error in estimation of lateral width can be judged by using the specification of the Olympus AC160TS cantilever (looking at figure 4.16) and the height of particles which the tip is scanning. The lever width is 50 μm and the tip radius is < 10 nm. We can approximately have an error between ±40 nm. The lateral error is large and thus we cannot expect to determine crystallite size with accuracy using AFM technique.

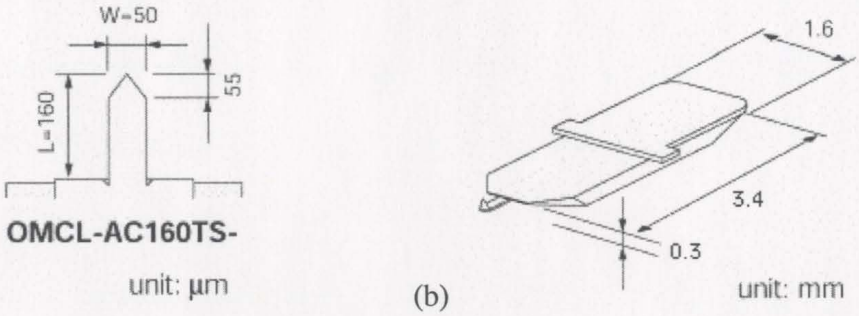

(a) (b)

Figure 4.16: Schematic of Olympus AC160TS showing dimensional details: (a) rectangular cantilever with tetrahedral tip, (b) Si cantilever showing the size of chip [39].

The AFM instrument was used to study various types of samples prepared by sphere-plate technique which included all three stages of film evolution. The AFM micrographs

confirm that there are round shaped particles (stage III samples) of Au present on the surface. Since we started with a uniform polycrystalline film (stage I), it is thus evident that the film broke along the grain boundaries when annealed at 530°C (stage II) and 920°C (stage III).

The micrographs distinguish variations in height of the round particles on the substrate. Observing the micrograph height, amplitude metric of all the samples, it appears that the height of the balls lie somewhere between 0.05 to 0.2 μms, this seems understandable as the film from which these balls are formed also lies in the same thickness range (~0.1 μms). The height distribution of Au particles varies between 0.05 to 0.2 μms.

AFM study can only be used to predict the relief features of the particles. Limitations exist in getting information about the interface as the scans are for the surface only and in predicting the shape of the particles accurately owing to low lateral accuracy. A better height resolution is an advantage over other characterization techniques like SEM, XRD etc., and there is no significant indication of faceting of Au particles.

From the SEM results, the approximate size distribution of faceted Au particles are between 0.05 to 0.2 μms. This combined with the height distribution from the AFM, 0.05 to 0.2 μms, indicates that the particles are very close to having a spherical shape of approximate average size 0.15 μms (from SEM).

4.5 Lattice Misfit Calculations

The lattice misfit can be expressed by the formula:

$$f = \frac{a_s - a_f}{a_f}$$

Where, a_s is the lattice parameter of substrate (Si) = 5.4309Å and a_f is the lattice parameter of the deposited film (Au) = 4.0786Å, [36]. Upon calculation using the above formula, we find that for 1x1 and 2x1 Au/Si system, the lattice misfit is as high as 33.156% and 33.422% respectively.

Table 4.8: Calculated misfit values for a few cubic crystal arrangements.

Au / Si system	**Misfit (%)**
1x1	33.156
2x1	33.422
3x2	11.229
4x3	0.133
5x4	6.524

From the table 4.8 above, one sees that the misfit value for 4x3 Au/Si system is the lowest and thus according to the theory behind geometric models, it is expected to show better epitaxial growth of Au film on Si substrate if it follows the 4x3 arrangement of cubic crystals.

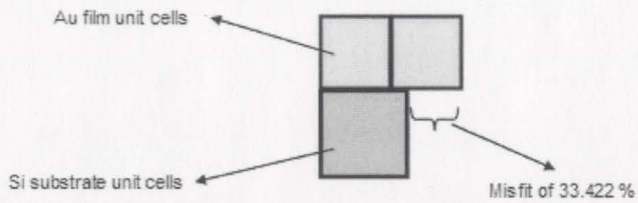

(a)

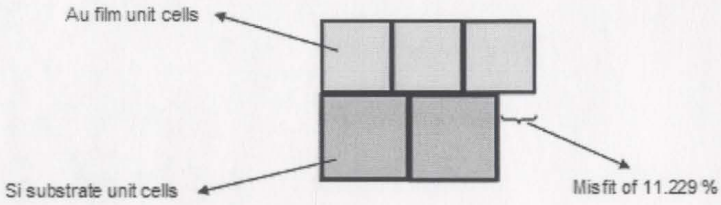

(b)

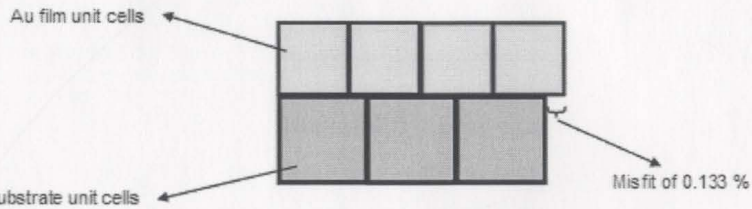

(c)

Figure 4.17: Schematic showing lattice misfit in different crystal arrangements: (a) 2x1, (b) 3x2 and (c) 4x3 Au/Si systems.

From the literature review, the CSL model seems to explain the lattice matching tendency of crystalline-crystalline interfaces. A Coincidence boundary is said to be at its lowest energy configuration when it lies in the most densely packed plane of the superlattice. The Au particles have therefore aligned into low energy configurations of preferred planes. This can be observed from the XRD data which shows preferred orientations taken by Au particles when annealed to intermediate and high temperature anneal stages.

The O-lattice suggests that Misfits between O-points is accommodated by dislocations by forming low energy structure, these points are the ones with minimum strain energies of exact matching between two interpenetrating lattices. The O-Lattice model like CSL model explains to some extent the reason for particles choosing to settle in certain preferred orientations.

DSC models suggests that regions of fit are patches of partial lattice matching across the boundary and the regions of misfit are line defects having dislocation, step or ledge character. Since the substrates Si(100) and Si(111) are grown tilted off axis by $\pm 0.5^{o}$, this would help the growth of thin films on the substrate due to the formation of steps and ledges which are regions of fit or matching enhancing the possibility of epitaxial growth.

4.6 Scherrer Formula Estimation of Crystallite Size

The Scherrer's formula approach can be used to estimate size of very small crystals from the measured width of their diffraction curves.

$$B = \frac{0.9\lambda}{t\cos\theta_B}$$

Where B is in radians, t is the average diameter of crystal, λ is the wavelength of the incident X-rays (Cu-K_α radiation = 1.54178 Å) and θ_B is the diffraction angle.

B is the breadth at half intensity maximum.

$$B = \frac{1}{2}(2\theta_2 - 2\theta_1).$$

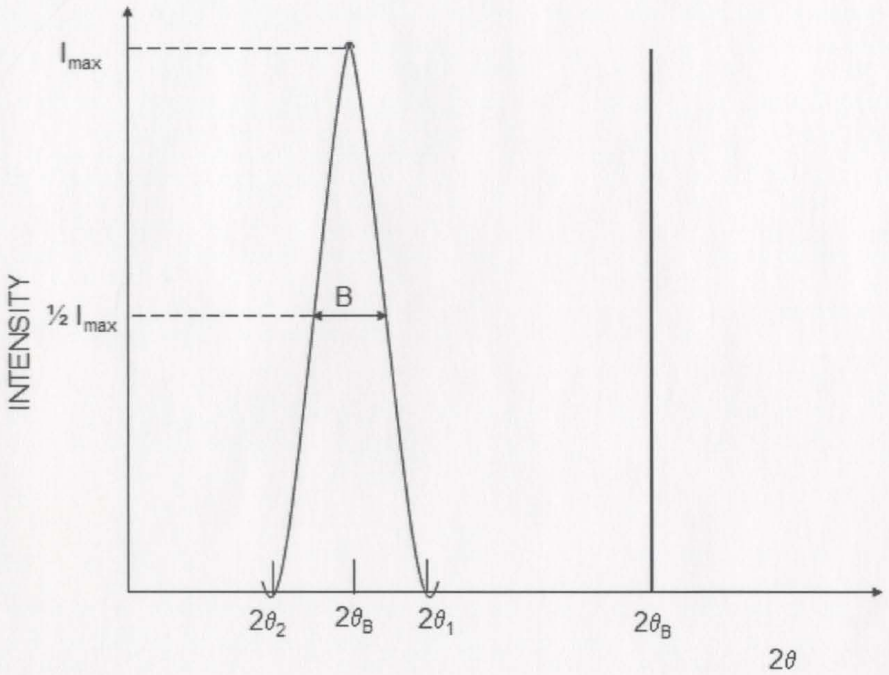

Figure 4.18: Diffraction curve showing peaks with different B values.

The crystal size is inversely proportional to the breadth at half-intensity maximum. The breadth is due to small crystal effect alone but the peak broadening is actually due to the crystal size as well as the machine broadening. Where the crystal size is determined from the data and the machine broadening is due to the error in the machine.

$$B = B_{(\text{average crystal size})} + B_{(\text{machine})}.$$

Neglecting $B_{(\text{machine})}$, assuming the peak broadening due to machine is negligible.

Table 4.9: Estimated crystallite size of Au using Scherrer's equation: in the stage III sphere-plate samples.

Substrate	**Crystal Size, t(μm)**
Si(100)	0.0934
Si(111)	0.0934
SiO_2	0.0989

The size of crystals or gold particles calculated from the Scherrer's formula are quiet different when compared with the ones estimated visually by statistical means from the SEM. Apart from being smaller than SEM picture values they are also very close to each other.

The Scherrer's equation is accurate only for particles in the range 0.05 to 0.2 μms [36]. Thus we are in the correct range to apply Scherrer's equation to our system and determine the particle size.

Scherrer's equation uses XRD data which is from a larger cross-section (>1mm^2) as compared to SEM picture which is only for 0.5 to 6 μms spot size cross-sections. Thus it is expected that XRD data should predict the crystal size to a higher degree of accuracy than SEM micrographs.

Chapter 5

Conclusions

1. Preferred orientations were measured for Au balls on Si(100), Si(111) and SiO_2 substrates and the most preferred orientation was found to be the closest-packed plane {111} for fcc Au. This low energy interface is the most stable due to the presence of close packed planes and directions. Additional preferred orientations were observed for Au{200} on Si(100) substrate and Au{200}, Au{220} and Au{311} on SiO_2 substrate.

2. These preferred orientations are low-energy configurations and corresponds to the cusps in the interfacial energy curve. As the annealing temperature was increased, the metal became more stable and rotated to form spheres of low energy orientation.

3. Long-range ordering of Au may be occurring across native oxide layers on Si(100) and Si(111) substrates to account for the epitaxial preferred orientation observed in each system.

4. SEM morphology gives a good 3D image of the Au balls with average lateral resolution between 0.05 to 0.2 μms. Photomicrographs shows both round shapes and the phenomena of faceting. It shows particles to round in shape.

5. AFM morphology gives a better height resolution (0.05 to 0.2 μms) rather than lateral resolution. The AFM image showed the Au particles to be nearly spherical in shape without indication of faceting.

6. Faceting of balls was observed from the SEM micrographs and it adheres to the Wulff construction argument. Faceting in amorphous-crystalline and crystalline-amorphous-crystalline systems confirm with Jackson's theory.

7. The lattice mismatch was calculated to be the lowest (0.133%) for the 4x3 configuration of Au on Si cubic crystals. It was found to be as low as 0.133 % for 4x3 type arrangement of cubic crystals.

8. Scherrer formula was used to determine Au crystal size and it was found to be between 0.05 to 0.2 μms, in tandem with the SEM and AFM estimations.

References

1. W. Lojkowski and H.-J. Fecht; *The structure of inter-crystalline interfaces, Progress in Mat. Sci.*; 45[5-6], (2000), 339-568.
2. V. Randle; *The role of the grain-boundary plane in cubic polycrystals, Acta Mat.*; 46[5], (1997), 1459-1480.
3. R.W. Balluffi and A.P. Sutton; *Why should we be interested in the atomic structure of interfaces; Mat. Sci. Forum*; 207-209, (1996), 1-12.
4. P. Lejcek and V. Paidar; *Intergranular and interphase boundaries in materials (iib98), Prague, 6-9 July, 1998, Mat. Sci. Forum*; 294-296, (1999), 1-840.
5. A.C. Ferro, J.P. Conde and M.A. Fortes; *Editors, Intergranular & Interphase Boundaries in Materials (iib95), Lisboa, June, 1995, Mat. Sci. Forum*; 207-209, (1996), 1-920.
6. A. P. Sutton and R. W. Balluffi; *Acta Met.*; 35(9), (1987), 2177.
7. G. A. Chadwick and D. A. Smith; *Grain Boundary Structure and Properties*; (1976).
8. D. G. Brandon, B. Ralph, S. Ranganathan and W. S. Wald; *Acta Met.*; 12, (1964), 813.
9. H. F. Fishmeister; *J. De Physique, Coll. C4*; 46, (1985), 3.
10. S. Ranganathan; *Acta Crystall.*; 21, (1966), 197.
11. J. M. Howe; *Interfaces in Materials, John Wiley & Sons, Inc.*; (1997).

12. W. Bollmann; *Crystal Defects and Crystalline Interfaces, Springer-Verlag, Berlin*; (1970)

13. Y. Ishida; *J. Mat. Sc.*; 7, (1972), 75.

14. D. A. Smith and R. C. Pond; *Int. Metals Rev.*; 205, (1976), 61.

15. P. H. Pumphrey; *Scripta Metall.*; 6, (1972),107.

16. J. A. Venables; *Introduction to Surface and Thin Film Processes, Cambridge University Press*; (2000).

17. C. Herring; *Phys. Rev.*; 82, (1951), 87-95.

18. C. Herring; *Structures and Properties of Solid Surfaces, Editors, R. Gomer and C.S. Smith, Chicago University Press*; (1953), 5-72.

19. A. P. Sutton and R. W. Balluffi; *Interfaces in Crystalline Materials, Oxford University Press*; (1995).

20. J. C. Heyraud and J. J. Metois; *Acta Metall.*; 28, (1980), 1789.

21. W. L. Winterbottom and N. A. Gjostein; *Acta Metall.*; 14, (1966), 1041.

22. J. W. Cahn; *Acta Metall.*; 8, (1960), 554.

23. K. A. Jackson; *Liquid Metals and Solidification, ASM, Cleveland, Ohio*; (1958), 174.

24. J. W. Cahn, W. B. Hillig and G. W. Sears; *Acta Metall.*; 12, (1964), 1421.

25. G. J. Shiflet; *Mat. Sci. and Eng.*; 81, (1986), 61.

26. W. T. Read and W. Shockley; *Imperfections in Nearly Perfect Crystals, John Wiley & Sons, NY*; (1952), 352.

27. P. Shewmon; *Recrystallization, Grain Growth and Textures*; (1966), 165.

28. H. Meiser and H. Gleiter; *Scripta Metall.*; 14, (1980), 95.

29. U. Erb and H. Gleiter; *Scripta Metall.*; 13, (1979), 61.

30. G. Herrmann, H. Gleiter and G. Bäro; *Acta Metall.*; 24, (1976), 329.

31. H. Sautter, H. Gleiter and G. Baro, *Acta Metall.;* 25, (1977), 467.

32. Y. Wakayama and S. Tanaka; *Journal of crystal growth*; 181, (1997), 304.

33. G. I. Distler, V. P. Vlasov and V. M. Kanevsky; *Thin Solid Films*; 33, (1976), 287.

34. K. L. Chopra; *J. Appl. Phys.*; 40, (1969), 906.

35. J. Shirokoff and U. Erb; *Scripta Metall.*; 20, (1986), 1607.

36. B. D. Cullity; *Elements of X-Ray Diffraction, second edition, Addison-Wesley*; (1978).

37. S. M. Sze; *VLSI Technolgy, McGraw-Hill Book Company*; (1983).

38. G. Binnig, C. F. Quate and C. H. Gerber; *Phys. Rev. Lett.*; 56(9), (1986), 930-933.

39. T. R. Albrecht, P. Grütter, D. Horne, and D. Rugar; *J. Appl. Phys.*; 69(2), (1991), 668-673.

40. http://www.asylumresearch.com/Products/Mfp3D/Mfp3D.shtml.

41. http://cmm.mrl.uiuc.edu/instruments/AFM/index.htm.

42. J. Shirokoff and U. Erb; *Thin Solid Films*; 151, (1987), 65.

43. J. Shirokoff J. Cheung and U. Erb; *Acta Metall. Mater.*; 38, (1990), 1273.

44. Y. Wakayama and S. Tanaka; *Nanostructured Materials*; 12, (1999), 13.

45. B. Satpati, P. V. Satyam, T. Som and B. N. Dev; *Appl. Phys. A*; 96, (2004), 447.

46. B. Satpati, P. V. Satyam, T. Som and B. N. Dev; *J. Appl. Phys.*; 96, (2004), 5212.

47. Y. F. Guan and A. J. Pedraza; *Nanotechnology*; 16, (2005), 1612-1618.

48. H. Hibino, Y. Watanabe; *Surface Science*; 588, (2005), L233-L238.

49. N. Arai, H. Tsuji, K. Ueno, T. Gotoh, K. Adachi, H. Kotaki, Y. Gotoh, J. Ishikawa; *Sharp technical Journal*; n91, (2005), 31.

50. N. Arai, H. Tsuji, K. Ueno, T. Matsumoto, Y. Gotoh, K. Adachi, H. Kotaki, J. Ishikawa; *Surface & Coatings Technology*; 196, (2005), 44-49.

51. X. Li, F. Huang, M. Curry, S. C. Street, M. L. Weaver; *Thin Solid Films*; 473, (2005), 164-168.

52. S. Sharma, T. I. Kamins and R. Stanley Williams; *Applied Physics A: Materials Science & Processing*; 80 (6), (2005), 1225-1229.